Eur. Phys. J. D **36**, 295–317 (2005)
DOI: 10.1140/epjd/e2005-00254-x

**The European
Physical Journal D**

Phase stability theory of Bloch eigenstates in active photonic lattices with coupled microlaser arrays

S. Riyopoulos[a]

Science Applications International Corporation, 1710 SAIC Dr. MS 2-2-2, McLean, VA 22102, USA

Received 4 October 2004 / Received in final form 3rd January 2005

Abstract. An generic model for the lattice dynamics of coupled microlaser arrays is employed for the lattice stability analysis. Nonlinear cross-cavity gain-coupling effects, characterizing active lattices, are included via the gain dependence on carrier depletion and cross-cavity hole burning. Passive near neighbor interactions (inter-cavity absorption and mirror reflection interference) are also included. The introduction of lattice-orthogonal modes simplifies the derivation of the coupled rate equations. The interaction phase among sites exhibits spontaneous long range "crystallization" into periodic Bloch states whereby the cavity radiation envelopes behave as laser "macro-atoms". The sign of the coupling coefficients as a function of geometry determines in- vs. out-of-phase locking and has practical implications for array design. Emphasis is placed on the stability analysis of Bloch states by including earlier omitted [1] effects of phase perturbations. The importance of the linewidth factor ι is uncovered: unconditional stability results for $\iota \leq 1$, otherwise a stability threshold exists for the coupling strength among sites. Choice of low ι gain material permits phase stability with high coupling strength, beneficial in overcoming manufacturing variations among array cavity parameters.

PACS. 42.55.Px Semiconductor lasers; laser diodes – 42.60.Fc Modulation, tuning, and mode locking – 42.60.Da Resonators, cavities, amplifiers, arrays, and rings

1 Introduction

Closely packed microlaser arrays, such as guided mode VCSEL cavities and active defect superlattices, interact through their evanescent fields, Figure 1. Fringe field interference during stimulated emission introduces cavity coupling, whereby photons confined in one cavity induce emission in neighboring cavities. The non-linear complex-gain dependence on carrier depletion and cross-cavity hole burning introduces *active* photonic lattice behavior. The photonic lattice resembles in certain aspects solid crystal behavior, whereby the radiation envelopes play the role of atomic wavefunctions.

The situation is distinctively different from well-known photonic bandgap materials involving strong, *passive* interactions through periodic dielectric interference [2,3]. Here weak but *active* evanescent field interference generates laterally propagating passbands out of localized, cavity-confined modes [4]. In that respect, it is the opposite limit from the strongly coupled photonic bandgap structures where interference among laterally propagating waves creates non-accessible frequency gaps inside a global continuum. By the same token it differs from amplified photonic modes [5,6] inside cavity arrays with gain, where the wave dispersion is primarily determined by passive interactions.

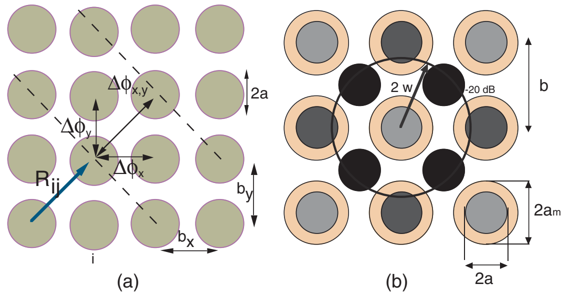

Fig. 1. Schematic 2-D array configuration. When phase-locked, the same phase difference applies between any two neighbors in the x- and in the y-direction (in general $\Delta\varphi_x \neq \Delta\varphi_y$). (b) Schematic interactions among near neighbors, a active region radius, a_m mirror radius, b center separation, w the $1/e^2$ mode waist. Solid black cicles mark passive absorption.

Earlier analytic studies of coupled laser arrays [7,8] neglected the carrier density evolution by using prescribed, fixed complex gain profiles. This eliminates the active cavity interactions, such as cross-cavity gain depletion (hole burning) and stimulated inter-cavity emission, and allows

---

[a] e-mail: `spilios.riyopoulos@saic.com`

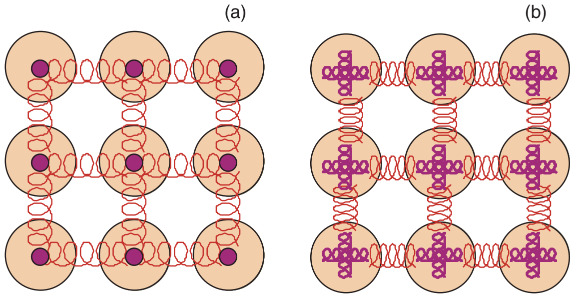

Fig. 2. Mechanical analogues (a) coupled passive cavity lattice: cavities behave as inertial masses coupled through weak springs (b) coupled active cavity lattice: cavities behave as oscillators of given eigenfrequency (thick inner springs), mutually coupled through weaker springs signifying lateral interactions The active oscillators are nonlinear, since frequency (i.e. "stiffness") depends on radiation amplitude.

only *linear* cavity coupling. Neglecting carrier depletion also eliminates the natural cavity oscillation frequency from the lattice dynamics. Other studies [9,10] included cross-cavity carrier depletion, but were limited to two coupled cavities. Thus they could not describe collective effects and lattice behavior. The stability dependence on coupling strength was noted [9,10], but the role of the the linewidth factor ι in determining conditional vs. unconditional stability was not recognized.

The presence of a characteristic cavity oscillation frequency Ω, due to interactions between the photon and the carrier populations, also differentiates from passively coupled cavities (coupled cavity waveguides [11,12]). One can draw an analogy with mechanical oscillators of "hard" inner spring constants $\Omega \propto \sqrt{k_{hard}}$ that are mutually coupled by soft springs $\sqrt{k_{soft}} \propto \sqrt{\Upsilon}$, as in Figure 2. The coupling strength Υ imposes phase synchronization and collective excitations; its smaller effect on the frequency $\Omega' \sim \Omega\sqrt{1+\Upsilon}$ determines the narrow bandwidth $\Delta\Omega$. The passive coupled cavity limit is the analogue of inertial masses coupled with a soft spring, where *both* the oscillation frequency and the coherence are generated by the spring action.

This work expands and revises earlier active lattice theory [1] in two important respects: it generalizes the lattice interactions and revises the stability of the collective lattice oscillations. Firstly, cross-cavity interactions are completed by including cross-cavity feedback from reflection interference among near cavity mirrors, periodic dielectric interference, and periodic passive absorption that is spatially anti-correlated to the gain distribution. The coupling coefficients are generalized for index-guided eigenmode profiles, due to thermal lensing, in addition to the gain-guided modes. More importantly, lattice stability is revised by including phase perturbations among sites, in addition to earlier addressed carrier density and radiation intensity perturbation [1]. The rigorous treatment uncovers the crucial importance of the linewidth factor ι: lattice stability is unconditional for $\iota \leq 1$, and subject to a coupling strength threshold otherwise.

The tight binding approximation for weak coupling is used, constructing composite lattice eigenmodes via superposition of phase-shifted single cavity eigenmodes [1]. The near-neighbor coupling coefficients for the lateral, phase-dependent interactions are obtained, representing cross-cavity gain depletion from stimulated emission, radiation feedback via mirror reflection interference, and passive dielectric variation interference. While lateral mode overlap stimulates additional radiation emission in adjacent cavities, the emitted radiation is also shared among those cavities since the original eigenmodes are not lattice-orthogonal. The net result is that, for weak overlapping, the gain coupling coefficients can be negative, even for positive, Gaussian mode profiles. This effect, which was not addressed earlier [1], is consistently included from the start by mode renormalization into lattice-orthogonal modes.

The dynamic lattice evolution is reduced to integration of the coupled cavity rate equations under appropriate boundary conditions (finite or periodic arrays). Starting from random initial conditions, the system settles into periodic steady states where the phase shift among neighbors scales as an inverse lattice vector $\Delta\Phi = \mathbf{K}\cdot\mathbf{b}$, Figure 1, manifesting phase crystallization into a standing Bloch wave. For an array of N identical cavities of period b, length $L = Nb$, any value $\Delta\Phi_n = 2\pi nb/L$ satisfies the phase locking $d\Delta\Phi_n/dt = 0$ among sites. We find that the lattice usually settles at steady-state values $\Delta\Phi_n = 0$, π that maximize the collective gain $\propto G_o \cos\Delta\Phi_n > 0$, where G_o embodies the sum of gain, absorption and interference coefficients.

The present analytic results offer insight for practical applications. Experiments [13–17] involving weakly coupled laser arrays with cavity-confined modes have shown a preference for spontaneous anti-phase locking $\Delta\Phi_n = \pi$. It is usually accepted that in-phase modes suffer higher losses between cavities, where absorption prevails, due to comparatively higher intensity there relative to anti-phased profiles. Gain computation using natural cavity modes, dividing the per-period gain overlap by the total per-period stored energy, indeed shows lower gain for in-phase modes, due to a higher fraction of radiation energy stored between cavities. Our lattice-orthogonal mode formalism automatically accounts for the "weighting" of the gain and losses by the per-period stored energy. The balance between gain and losses is reflected in the overall coupling factor G_o, summing up gain, reflection and absorption. Competition between cross-cavity stimulated emission and cross-cavity photon sharing can turn the gain coupling and G_o negative, even for positive (Gaussian) cavity mode profiles. Negative collective coupling $G_o < 0$ yields lower in-phase gain, favoring anti-phasing. To achieve $G_o > 0$ and in-phase locking, preferable for many practical applications, our analysis suggests two ways. One is to increase constructive inter-cavity reflection interference, by increasing the Bragg mirror reflectivity *between* cavities. The other is reducing the cavity separation b relative to the modal waist w, since positive gain overlap and $G_o > 0$ result for $w/b \sim 1$. Stability considerations become important as cavities get closer: the coupling strength cannot exceed a small threshold unless we operate in the unconditional stability regime $\iota \leq 1$. Most III-V semiconductors have bulk material value $\iota \simeq 2$–3; however quantum dots and dots in quantum wells have recently shown $\iota \simeq 1$.

For finite arrays we observe boundary layer formation at steady state, where cavity densities and intensities vary with the distance from the edges [21]. Drawing again the analogy with mechanical springs, the nonlinear lattice responds to the boundary conditions by changing the edge cavity "spring constants", i.e. the intensity-dependent cavity frequencies, in addition to phase selection that is the only option in linear lattices.

The dynamics of collective phase oscillations around a steady state lattice, subject to constant drive biases, is further analyzed. The unconditional stability regime for $\iota \equiv g_i/g_r$ yields a dispersion of stable, time decaying collective oscillations. Local site excitation with a real frequency bias leads to space-decaying lattice waves. These coherent, low frequency coupled variations among the photon and carrier densities constitute a "photonic sound" analogue for active lattices. For $\iota > 1$ the stability is conditional and depends on the coupling strength Υ. At larger coupling strengths we observe transition to limit cycles, tantamount to self-excitation of photonic sound under constant in time biases. At even higher coupling we observe transition to chaotic behavior, typical of nonlinear dissipative systems. An interesting aspect is that instability follows not by increasing the external gradient (drive voltages for the laser cavities) but by increasing the system "cohesiveness" (cavity coupling strengths.)

2 Rate equations for coupled VCSEL cavities

In Figure 1 we assume that $M \times N$ identical cavities are arranged in the $(x-y)$-plane with axes along the z-direction and thin circular active areas centered at the lattice vectors $\mathbf{R}_{ij} = i\mathbf{b}_x + j\mathbf{b}_y$ with $\mathbf{b}_x$, $\mathbf{b}_y$ basis vectors. The complex gain distribution reflects the periodic electron-hole pair density $\mathcal{N}$ in the active regions

$$\mathcal{N}(\mathbf{r}) = \sum_{i,j} N_{ij}(t)\chi(\mathbf{r} - \mathbf{R}_{ij}) \tag{1}$$

where N_{ij} is the cross-section averaged density and $\chi(\mathbf{r})$ its normalized profile, as shown in Figure 3a. We include index-guiding effects allowing spatial variation in the real part of the dielectric constant

$$\epsilon^r(\mathbf{r}) = \epsilon^r_o + \sum_{i,j} \delta\epsilon^r(\mathbf{r} - \mathbf{R}_{ij}) \tag{2}$$

where the uniform background ϵ_o is the bound electron response. The induced dielectric corrections are limited within effective radius a (taken equal to the carrier density and current radius), Figure 3b. The two dielectric terms inside

$$\delta\epsilon^r(\mathbf{r}) = -\frac{\omega_p^2}{\omega^2}\chi(\mathbf{r}) + \frac{a^2 - \mathbf{r}^2}{W^2} \tag{3}$$

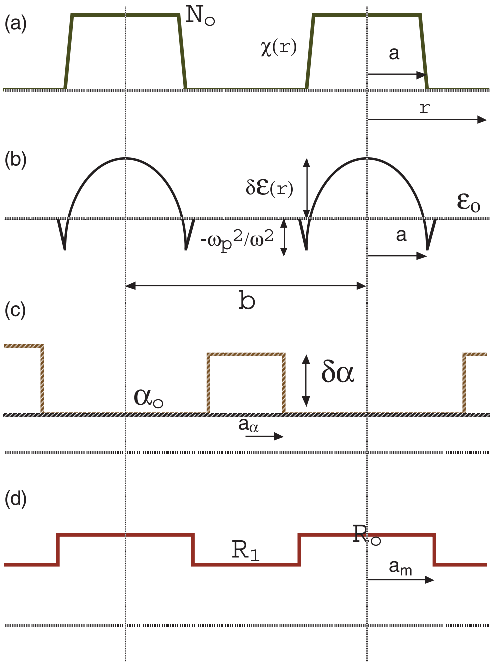

Fig. 3. Profiles of (a) carrier density (gain), (b) real dielectric constant, (c) passive absorption and (d) mirror reflectivity, along a 1-D lattice cross-section.

give, respectively, the free carriers dielectric response (negative, anti-guiding) where $\omega_p^2 = 4\pi N_{th} e^2/m^*$ is the plasma frequency with $1/m^* = 1/m_e^* + 1/m_h^*$, and the thermally induced on-axis index peaking (guiding), which is taken parabolic in radius and relatively shallow $a/W \ll 1$. The overall effect is guiding for $a^2/W^2 > \omega_p^2/\omega^2$. The temperature is assumed constant, neglecting transients in the dielectric response. The passive absorption profile is defined by the absorption coefficient $\alpha(\mathbf{r}) \equiv \omega\epsilon^i(\mathbf{r})/v_g$ where ϵ^i is the imaginary part of the dielectric constant. In most practical cases, the spatial distribution of absorption is anticorrelated with gain and index; it centers around halfway-lattice points, Figure 3c,

$$\epsilon^i(\mathbf{r}) = \epsilon^i_o + \delta\epsilon^i \sum_{i,j} \chi_\alpha(\mathbf{r} - \mathbf{R}^\dagger_{ij}) \tag{4}$$

defined by $\mathbf{R}^\dagger_{ij} = (i \pm 1/2)\mathbf{b}_x + (j \pm 1/2)\mathbf{b}_y$. Dielectric effects, dominated by carrier density and temperature, peak inside cavities; absorption peaks between cavities, due to subthreshold carrier densities there. This accounts for the different spatial distributions of ϵ^r, ϵ^i

Finally, the spatial variation in the reflectivity among cavity DBRs R_o and background material R_1, shown in Figure 3d, is given by

$$R(\mathbf{r}) = R_o \sum_{i,j} \psi(\mathbf{r} - \mathbf{R}_{ij}) + R_1 \sum_{i,j} [1 - \psi(\mathbf{r} - \mathbf{R}_{ij})] \tag{5}$$

where R_o, R_1 stand for combined roundtrip reflectivity in the vertical z-direction, which may also incorporate diffraction and scattering losses. Without loss of generality a cylindrically uniform step-function profile is assumed for both χ, ψ,$\chi(\mathbf{r}) = 1$, $r \leq a$, $\psi(\mathbf{r}) = 1$, $r \leq a_m$ and zero otherwise, normalized so that $(1/\pi a^2)\int d\mathbf{r}^2 \chi(\mathbf{r}) = (1/\pi a_m^2)\int d\mathbf{r}^2 \psi(\mathbf{r}) = 1$.

For weakly coupled cavities, involving laterally confined modes interacting through their fringe fields, the radiation field is expressed as a linear superposition of localized cavity modes (tight-binding approximation), of slowly varying complex amplitudes $\mathcal{E}_{ij}(t)$ and eigenmode envelopes $U^{mp}(\bar{\mathbf{r}})$ centered around lattice vectors $\bar{\mathbf{r}} = \mathbf{r} - \mathbf{R}_{ij}$

$$\mathbf{E} = \sum_{i,j}\sum_{m,p} \mathcal{E}_{ij}^{mp}(t) U^{mp}(\mathbf{r} - \mathbf{R}_{ij}) e^{i(kz - \omega_{mp} t)}. \qquad (6)$$

For the assumed parabolic index profile, (3), the transverse mode envelopes are given by Gauss-Laguerre functions $U^{mp}(\sqrt{2}r/w)$ with modal waist $w = \sqrt{Wc/\omega}$. In addition to the usual orthonormality among same cavity eigenmodes $\int d^2\mathbf{r} U^{mp*}(\mathbf{r}) U^{nq}(\mathbf{r}) = \delta^{mn}\delta_{pq}$ it is convenient to impose spatial orthonormality among same modal profiles m, p around different lattice sites. While the U-basis is not lattice-orthogonal, a new $\hat{U}$ orthogonal basis follows via the Gram-Schmidt algorithm (Appendix A), so that

$$\int d^2\mathbf{r} \hat{U}^*(\mathbf{r} - \mathbf{R}_{ij}) \hat{U}(\mathbf{r} - \mathbf{R}_{i'j'}) = \delta_{i,i'}\delta_{j,j'}. \qquad (7)$$

Since eventually we will consider only next-neighbor interactions we limit orthonormalization to $\mathbf{R}_{ij} - \mathbf{R}_{i'j'} = \pm\mathbf{b}_{x,y}$ by defining (Appendix A)

$$\hat{U}(\mathbf{r}) = U(\mathbf{r}) - \frac{1}{2N_D}\sum_{\pm x}\sum_{\pm y} C_{x,y} U(\mathbf{r} \mp \mathbf{b}_{x,y}) \qquad (8)$$

where N_D is the dimensionality of the array and the next neighbor projection coefficients $C_{x,y}$ are given by

$$C_{x,y} = \int_0^\infty d^2 r U^*(\mathbf{r}) U(\mathbf{r} \mp \mathbf{b}_{x,y}) = e^{-\frac{b_{x,y}^2}{2w^2}}. \qquad (9)$$

Comparison of fundamental Gaussian profiles with their lattice-orthogonal counterparts is shown in Figure 4 for various lattice period values b/w. To satisfy (7) the lattice-orthogonal $\hat{U}$ have negative tails for $r \geq b$, thus overlap products between sites are negative, Figure 5. This will affect the sign of radiation coupling coefficients later on. Orthonormality among the density/gain profiles χ follows automatically by assuming that cavities do not "touch", $b_{x,y} > 2a$, whence

$$\int d^2 r \chi^*(\mathbf{r} - \mathbf{R}_{ij}) \chi(\mathbf{r} - \mathbf{R}_{i'j'}) = 0. \qquad (10)$$

We assumed the same electric field polarization $\hat{\mathbf{e}}$ for all cavities, aligned with $\hat{\mathbf{x}}$. The uniform medium dispersion is $\omega_{mp} = k_{mp} c/\sqrt{\epsilon_o}$ where k_{mp} is defined by the cavity resonance $k_{mp} = (2\pi + \psi_{mp})/L$, including the phase correction ψ_{mp} from complex reflection. The sought after photonic modulation frequency is near the natural cavity oscillation frequency, $(d/dt)\ln\mathcal{E} \simeq \Omega$, usually much

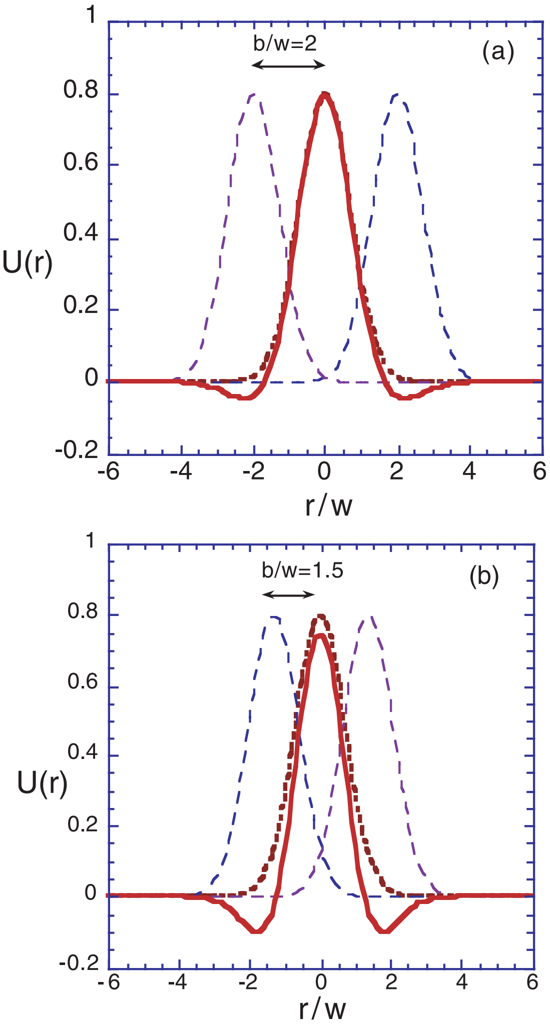

Fig. 4. Cavity eigenmode profiles (dashed) and the resulting lattice-orthogonal eigenmodes (solid) for given Gaussian waist w and with decreasing cavity separation b; (a) $b/w = 2$, (b) $b/w = 1.5$. Orthogonalized mode functions have opposite signs at overlap regions.

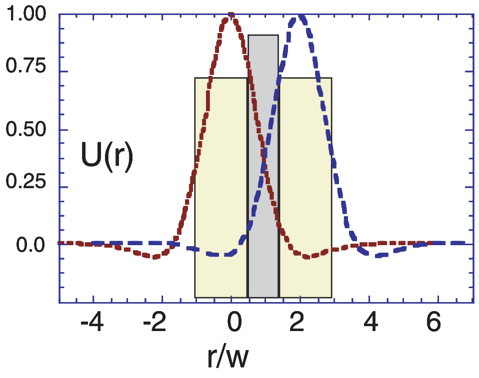

Fig. 5. Origin of negative sign of coupling coefficients for positive (Gaussian) cavity eigenmodes. The lattice-orthogonalized mode functions have opposite signs over the gain regions (light shaded) yielding negative gain-coupling coefficients Υ, Λ, and similar for mirror reflection interference. Same sign overlap over half-lattice regions (heavy shaded) yields positive absorption coupling coefficients V, Π.

smaller than the frequency separation among cavity modes $\omega_{mp} - \omega_{m'p'}$. Thus one can ignore resonant coupling between cross-modal beating $\Delta\omega_{mp}$ and lattice oscillations, and pick a single mode mp; without loss of generality we choose the fundamental $m = 0, p = 0$ and $U \equiv U_{oo}$.

Substituting (6) in the wave equation, factoring the fast phase term $e^{ikz-i\omega t}$ out, and keeping lowest order terms in the time derivative $d\mathcal{E}/dt$ yields

$$\sum_{ij} \mathcal{E}_{ij} \left[\nabla_\perp^2 - k^2 + \frac{\omega^2}{c^2} \left(\epsilon_o^r + \delta\epsilon^r(\mathbf{r} - \mathbf{R}_{ij}) \right) \right] \hat{U}(\mathbf{r} - \mathbf{R}_{ij}) + \sum_{ij} \mathcal{E}_{ij} \frac{\omega^2}{c^2} \left[\Delta\epsilon_{ij}^r(\mathbf{r}) + i\Delta\epsilon_{ij}^i(\mathbf{r}) \right] \hat{U}(\mathbf{r} - \mathbf{R}_{ij}) - \sum_{ij} \hat{U}(\mathbf{r} - \mathbf{R}_{ij}) \frac{2i\omega}{c^2} \epsilon \frac{\partial \mathcal{E}_{ij}}{\partial t} = \sum_{ij} \frac{4\pi\omega^2}{c^2} \mathcal{P}_{ij}. \quad (11)$$

The ijth site experiences the influence of all other sites through the terms $\Delta\epsilon_{ij}^r(\mathbf{r}) \equiv \sum_{i',j' \neq i,j} \delta\epsilon^r(\mathbf{r} - \mathbf{R}_{i'j'})$ and $\Delta\epsilon_{ij}^i(\mathbf{r}) \equiv \sum_{i',j'} \delta\epsilon^i(\mathbf{r} - \mathbf{R}_{i'j'}^\dagger)$ given in (2–4). We now apply the index-guided cavity eigenmode definition to the first line

$$\left[\nabla_\perp^2 - k^2 + \frac{\omega^2}{c^2} \left(\epsilon_o^r + \delta\epsilon^r(\mathbf{r}) \right) \right] \hat{U}(\mathbf{r}) = 0. \quad (12)$$

(Letting $\delta\epsilon^r = 0$ yields the paraxial wave equation for gain-guided diffraction limited modes used in [1]). Although, strictly speaking, it is the original "unhatted" modes U that exactly satisfy (12), the corrections from the normalization $\hat{U}$ are of second order in the coupling parameters (Appendix A) and thus neglected. Hence the slow envelope equation becomes

$$\sum_{ij} \hat{U}(\mathbf{r} - \mathbf{R}_{ij}) \left(\frac{\partial \mathcal{E}_{ij}}{\partial t} - i\frac{\omega}{2} \frac{\Delta\epsilon_{ij}^r(\mathbf{r})}{\epsilon_o} \mathcal{E}_{ij} + \frac{v_g}{2} \frac{\Delta\alpha_{ij}(\mathbf{r})}{\epsilon_o} \mathcal{E}_{ij} \right) = -\frac{4\pi i}{2\epsilon_o} \omega \sum_{ij} \mathcal{P}_{ij}(\mathbf{r}) \quad (13)$$

where we defined the absorption coefficient $\Delta\alpha \equiv \omega\Delta\epsilon^i / v_g$. The polarization $\mathcal{P} \propto \mathcal{E}$ on the right-hand side is related to the induced dipole moment during stimulated emission $p = \mathbf{p} \cdot \hat{\mathbf{e}}$, where $\mathbf{p} = \langle e | e\mathbf{r} | h \rangle$ signifies transition between the electron $\langle e|$ and hole $|h\rangle$ states. The evolution of the complex electric field amplitude in a given cavity is obtained from the integral projection of (13) with the $U(\mathbf{r} - \mathbf{R}_{ij})$ wavefunction, taking advantage of the orthonormality (7), and using the microscopic transition elements $p(\omega)$, yielding [1]

$$\frac{\partial \mathcal{E}_{ij}}{\partial t} = \frac{2\pi p^2}{\epsilon_o \hbar} \frac{\omega(\Gamma - i\Delta\omega)}{\Delta\omega^2 + \Gamma^2} \zeta \left[Q_{ij} \mathcal{N}_{ij} \mathcal{E}_{ij} + \sum_{i' \neq i, j' \neq j} \Lambda_{ij;i'j'} \mathcal{N}_{i'j'} \mathcal{E}_{ij} + \Upsilon_{ij;i'j'} \left(\mathcal{N}_{ij} \mathcal{E}_{i'j'} + \mathcal{N}_{i'j'} \mathcal{E}_{i'j'} \right) \right] + i\frac{\omega}{2} \delta\hat{\epsilon} \left[Q_{ij} \mathcal{E}_{ij} + \sum_{i' \neq i, j' \neq j} \Lambda_{ij;i'j'} \mathcal{E}_{ij} + 2\Upsilon_{ij;i'j'} \mathcal{E}_{i'j'} \right] - \frac{v_g}{2} \delta\hat{\alpha} \left[\sum_{i' \neq i, j' \neq j} \Pi_{ij;i'j'} \mathcal{E}_{ij} + 2V_{ij;i'j'} \mathcal{E}_{i'j'} \right]. \quad (14)$$

Above $\Delta\omega$ is the frequency difference from resonance $\hbar\omega_o = E_e - E_h$ and Γ the phenomenological linewidth broadening. We also defined $\delta\hat{\epsilon} \equiv \delta\epsilon^r / \epsilon_o$ and $\delta\hat{\alpha} \equiv \delta\alpha / \epsilon_o$. The evolution of the carrier density (i.e. population inversion $\mathcal{N} = \rho_{ee} - \rho_{hh}$) in the ijth cavity is obtained in a similar manner [1], via the integral projection of the global carrier density equation with $\chi(\mathbf{r} - \mathbf{R}_{ij})$,

$$\frac{\partial \mathcal{N}_{ij}}{\partial t} = \frac{J_{ij}}{ed_w} - \gamma \mathcal{N}_{ij} - \left(\frac{p}{\hbar} \right)^2 \frac{\Gamma}{\Delta\omega^2 + \Gamma^2} \times \left[\mathcal{N}_{ij} \mathcal{E}_{ij} \mathcal{E}_{ij}^* + \sum_{i' \neq i, j' \neq j} \Lambda_{ij;i'j'} \mathcal{N}_{ij} \mathcal{E}_{i'j'} \mathcal{E}_{i'j'}^* + \sum_{i' \neq i, j' \neq j} \left(\Upsilon_{ij;i'j'} \mathcal{N}_{ij} \mathcal{E}_{i'j'} \mathcal{E}_{ij}^* + cc \right) \right] \quad (15)$$

where the the step-function property $\chi^2(\mathbf{r}) = \chi(\mathbf{r})$ for the uniform carrier density profile in each cavity was used. Three kinds of coefficients enter the above equations. The transverse confinement factor

$$Q_{ij} = \int_0^\infty d^2\mathbf{r} \hat{U}^*(\mathbf{r} - \mathbf{R}_{ij}) \chi(\mathbf{r} - \mathbf{R}_{ij}) \hat{U}(\mathbf{r} - \mathbf{R}_{ij}) \quad (16)$$

yields the transverse radiation overlap with the gain medium in an isolated cavity; the "longitudinal confinement" factor $\zeta = (d_w / L)$ has also been factored out. The inter-cavity coupling strengths are given by the following two coefficients

$$\Lambda_{i'-i,j'-j} = \int_0^\infty d^2\mathbf{r} \hat{U}^*(\mathbf{r} - \mathbf{R}_{ij}) \chi(\mathbf{r} - \mathbf{R}_{i'j'}) \hat{U}(\mathbf{r} - \mathbf{R}_{ij}) \quad (17)$$

$$\Upsilon_{i'-i,j'-j} = \int_0^\infty d^2\mathbf{r} U^*(\mathbf{r} - \mathbf{R}_{ij}) \chi(\mathbf{r} - \mathbf{R}_{ij}) U(\mathbf{r} - \mathbf{R}_{i'j'}). \quad (18)$$

The dielectric interference coefficients have also been expressed in terms of Υ, Λ as $\delta\hat{\epsilon}^r \Upsilon_{i'-i,j'-j}$, by redefining the effective $\delta\epsilon^r$

$$\delta\hat{\epsilon}^r = \frac{\int_0^\infty d^2\mathbf{r} U^*(\mathbf{r} - \mathbf{R}_{ij}) \delta\epsilon(\mathbf{r} - \mathbf{R}_{i'j'}) \chi(\mathbf{r} - \mathbf{R}_{i'j'}) U(\mathbf{r} - \mathbf{R}_{ij})}{\int_0^\infty d^2\mathbf{r} U^*(\mathbf{r} - \mathbf{R}_{ij}) \chi(\mathbf{r} - \mathbf{R}_{i'j'}) U(\mathbf{r} - \mathbf{R}_{ij})}. \quad (19)$$

We assume that the absorption distribution peaks halfway between cavities and is spatially anti-correlated with the gain and radiation profiles. For uniform absorption profiles $\chi_\alpha = 1$ of radius a_α, centered around half-lattice points $\mathbf{R}^\dagger_{i'j'} = \mathbf{R}_{i'j'} - \mathbf{b}/2$, the overlap factors between radiation and absorption are given by

$$\Pi_{i'-i,j'-j} = \int_0^\infty d^2\mathbf{r}\hat{U}^*(\mathbf{r}-\mathbf{R}_{ij})\chi_\alpha(\mathbf{r}-\mathbf{R}^\dagger_{i'j'})\hat{U}(\mathbf{r}-\mathbf{R}_{ij}) \tag{20}$$

$$V_{i'-i,j'-j} = \int_0^\infty d^2\mathbf{r}\hat{U}^*(\mathbf{r}-\mathbf{R}_{ij})\chi_\alpha(\mathbf{r}-\mathbf{R}^\dagger_{ij})\hat{U}(\mathbf{r}-\mathbf{R}_{i'j'}) \tag{21}$$

Π, V have a different functional dependence from Υ, Λ.

Due to periodicity the coupling coefficients depend only on the separation distance $\Delta\mathbf{R}_{i-i',j-j'} = \mathbf{R}_{ij} - \mathbf{R}_{i'j'}$ among lattice sites, implying parallel translation invariance $\Lambda_{ij;i'j'} \equiv \Lambda_{i'-i,j'-j}$, $\Upsilon_{ij;i'j'} \equiv \Upsilon_{i'-i,j'-j}$ etc. Thus, one may substitute $\hat{U}^*(\mathbf{r}-\mathbf{R}_{ij})\chi(\mathbf{r}-\mathbf{R}_{i'j'}) \to \hat{U}^*(\mathbf{r})\chi(\mathbf{r}-\Delta\mathbf{R}_{i'-i,j'-j})$ and $\hat{U}^*(\mathbf{r}-\mathbf{R}_{ij})\chi_\alpha(\mathbf{r}-\mathbf{R}^\dagger_{i'j'}) \to \hat{U}^*(\mathbf{r}-\Delta\mathbf{R}_{i'-i,j'-j})\chi_\alpha(\mathbf{r}-\mathbf{b}/2)$ for the coefficient computation. The Hermitian property is also satisfied, taking the form $\Lambda^*_{i-i',j-j'} = \Lambda_{i'-i,j'-j}$ etc.

The terms $\Lambda_{ij;i'j'}$ and $\Upsilon_{ij;i'j'}$ represent distinctively different interactions [1]. Specifically, the total induced polarization in each cavity is the vector sum of the response to its own electric field plus its adjacent cavity, phase shifted fields. The cross-polarization $\Upsilon_{ij;i'j'}$ mitigates the coupling of the self-induced polarization in one site to the fields of its neighbor sites and introduce the phase dependence. The cross-gain $\Lambda_{ij;i'j'}$ mitigates interactions where the polarization induced by one site to its neighbors couples back into the gain of the original site, and is phase independent. Similar reasoning yields both phase dependent and independent terms, $V_{ij;i'j'}$ and $\Pi_{ij;i'j'}$ respectively, from the passive absorption $\delta\hat{\alpha}$. The refraction coupling strengths are also given by $\Lambda_{ij;i'j'}$ and $\Upsilon_{ij;i'j'}$ from the geometrical similarity of $\delta\epsilon$ and the gain profiles.

We now need to introduce the boundary conditions in the axial direction z from mirror reflections, which can cause inter-cavity mirror feedback interference [8]. One effective reflection takes place every cavity roundtrip, and the reflected field is given according to (5)

$$\begin{aligned}\mathbf{E}^\dagger &= \sum_{i,j}\mathcal{E}^\dagger_{ij}U(\mathbf{r}-\mathbf{R}_{ij})\\ &= R(\mathbf{r})\sum_{i,j}\mathcal{E}_{ij}U(\mathbf{r}-\mathbf{R}_{ij}).\end{aligned} \tag{22}$$

Diffraction and scattering losses may also be incorporated inside R [18]. The phase shift during round-trip has been absorbed into the definition of the resonant cavity wavelength k_z and the cavity frequency ω_o. Taking the projection onto the ij mode profile yields

$$\begin{aligned}&\mathcal{E}^\dagger_{ij}/\mathcal{E}_{ij} \equiv \mathcal{R}\\ &\quad = R_o\sum_{i,j}\left[Q^m_{ij} + \sum_{i'\neq i,j'\neq j}\left(\Lambda^m_{ij;i'j'} + 2\Upsilon^m_{ij;i'j'}\mathcal{E}_{i'j'}/\mathcal{E}_{ij}\right)\right]\\ &\quad + R_1\sum_{i,j}\left[(1-Q^m_{ij}) - \sum_{i'\neq i,j'\neq j}\left(\Lambda^m_{ij;i'j'} + 2\Upsilon^m_{ij;i'j'}\mathcal{E}_{i'j'}/\mathcal{E}_{ij}\right)\right]\end{aligned} \tag{23}$$

The coefficients $Q^m, \Lambda^m, \Upsilon^m$ are defined exactly as in (16, 17), except the superscript ^{m} reflects the mirror radius value a_m that in general differs from the gain region a. In order to distribute the round-trip losses over the round trip time $2L/v_g$ where $v_g \cong c/\sqrt{\epsilon_o}$ we set $\mathcal{E}^\dagger_{ij} = \exp[-\mu(\mathbf{r})v_g t]\mathcal{E}_{ij}$ and define

$$\begin{aligned}\mu(\mathbf{r}) &\equiv -\frac{\ln(\mathcal{E}^\dagger_{ij}/\mathcal{E}_{ij})}{2L}\\ &= \frac{\mu^o_{ij}}{2}\left[1 - \sum_{i'\neq i,j'\neq j}\left(\Lambda^\dagger_{ij;i'j'} + \Upsilon^\dagger_{ij;i'j'}\mathcal{E}_{i'j'}/\mathcal{E}_{ij}\right)\right],\end{aligned} \tag{24}$$

with $\mu^o_{ij} \equiv -\ln[R_oQ_{ij} + R_1(1-Q_{ij})]^2/2L$ the single cavity reflection losses (power), allowing for non-zero reflectivity R_1 outside the mirror. The terms, defined by $\Lambda^\dagger_{ij;i'j'} = \xi\Lambda^m_{ij;i'j'}\Upsilon^\dagger_{ij;i'j'} = \xi\Upsilon^m_{ij;i'j'}$ describe coupling through reflection interference from nearby cavity mirrors. Note that for given geometry the sign of coupling depends on the difference between mirror and ambient reflectivity via $\xi \equiv (1-R_1/R_0)/2Q_{ij}L\mu_o$. Thus negative overlap $\Lambda^m_{ij;i'j'} < 0$ can produce positive $\Lambda^\dagger_{ij;i'j'} > 0$ and in-phase (constructive) reflection coupling that reduces losses when the ambient material reflectivity is higher than the mirror $R_1 > R_o$. Eventually the round trip mirror loss is equivalent to the time derivative $\mathcal{E}_{ij}\partial\mathcal{R}/\partial t = -v_g\mu(\mathbf{r})\mathcal{E}_{ij}$, added to the rhs of the complex amplitude equation,

$$\begin{aligned}&\frac{\partial\mathcal{E}_{ij}}{\partial t} =\\ &\frac{2\pi p^2}{\epsilon_o\hbar}\frac{\omega(\Gamma - i\Delta\omega)}{\Delta\omega^2+\Gamma^2}\zeta\left[Q_{ij}\mathcal{N}_{ij}\mathcal{E}_{ij} + \sum_{i'\neq i,j'\neq j}\Lambda_{ij;i'j'}\mathcal{N}_{i'j'}\mathcal{E}_{ij}\right.\\ &\left. +\Upsilon_{ij;i'j'}\left(\mathcal{N}_{ij}+\mathcal{N}_{i'j'}\right)\mathcal{E}_{i'j'}\right] - v_g\frac{\mu}{2}\left[\mathcal{E}_{ij} - \sum_{i'\neq i,j'\neq j}\Lambda^\dagger_{ij;i'j'}\mathcal{E}_{ij}\right.\\ &\left. +2Y^\dagger_{ij;i'j'}\mathcal{E}_{i'j'}\right] - \frac{v_g}{2}\delta\hat{\alpha}\left[\sum_{i'\pm i,j'\pm j'}\Pi_{ij,i'j'}\mathcal{E}_{ij} + 2V_{ij;i'j'}\mathcal{E}_{i'j'}\right]\\ &+i\frac{\omega}{2}\delta\hat{\epsilon}\left[Q_{ij}\mathcal{E}_{ij} + \sum_{i'\neq i,j'\neq j}\Lambda_{ij;i'j'}\mathcal{E}_{ij} + 2\Upsilon_{ij;i'j'}\mathcal{E}_{i'j'}\right],\end{aligned} \tag{25}$$

where, for uniform lattice parameters, $\mu_{ij} = \mu$. This is a general set of equations describing active cavity coupling

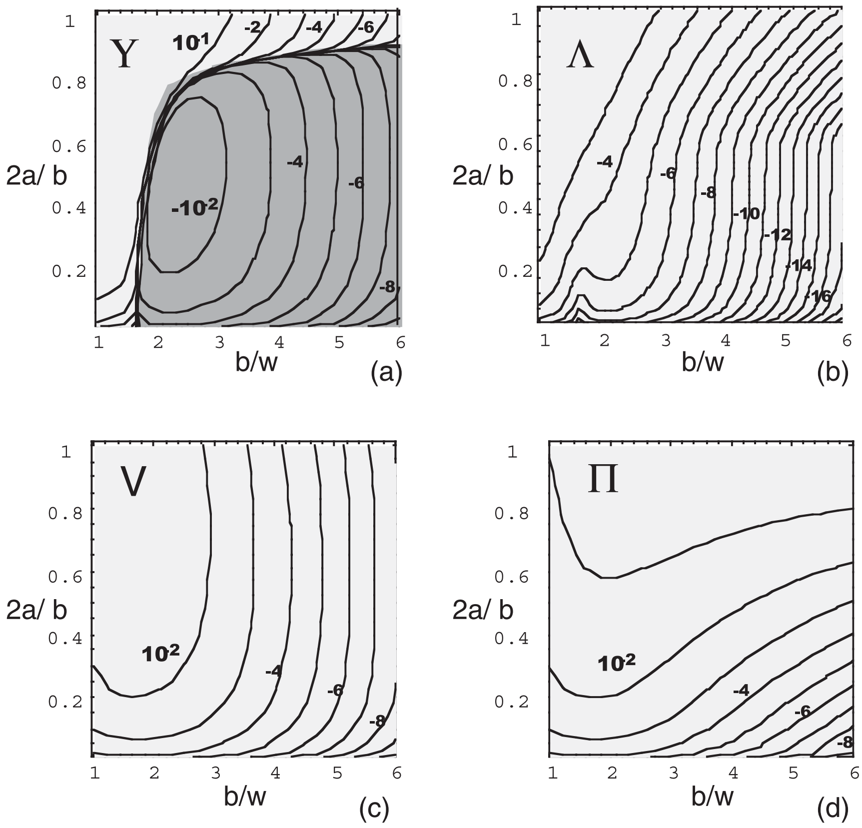

Fig. 6. Dependence of coupling coefficient strength on lattice geometry. Contour plots of (a) Υ, (b) Λ, (c) V and Π vs. cavity radius-to-separation $2a/b$ and separation-to-mode waist b/w. Contour values vary exponentially as 10^{-X}. Darks areas signify negative coupling values.

from cross-polarization gain, as well as passive coupling from index variation, passive ambient absorption and reflection interference feedback.

Cross-current leakage among neighboring cavities, as well as long-range thermal coupling are neglected, since the characteristic times for carrier and heat diffusion are much longer than the optical coupling time and the $1/\Omega$ period.

3 Nearest neighbor coupled array model

For fast decay of the localized radiation envelope $U(\mathbf{r})$ only the nearest site interactions need be retained, with $i' = i \pm 1$, $j' = j \pm 1$. All relevant coefficients are then reduced to the values, $Q_{ij} = Q$, $\Lambda_{i,j;i\pm1,j} = \Lambda_{i,j;i,j\pm1} = \Lambda$, $\Upsilon_{i,j;i\pm1,j} = \Upsilon_{i,j;i,j\pm1} = \Upsilon$, $\Pi_{i,j;i\pm1,j} = \Pi_{i,j;i,j\pm1} = \Pi$, $V_{i,j;i\pm1,j} = V_{i,j;i,j\pm1} = V$, given by the following geometrical overlap factors

$$Q = \int_0^\infty d^2\mathbf{r}\hat{U}^*(\mathbf{r})\chi(\mathbf{r})\hat{U}(\mathbf{r}), \tag{26}$$

$$\Upsilon = \int_0^\infty d^2\mathbf{r}\hat{U}(\mathbf{r})\chi(\mathbf{r})\hat{U}(\mathbf{r}-\mathbf{b}) \tag{27}$$

$$\Lambda = \int_0^\infty d^2\mathbf{r}\hat{U}^2(\mathbf{r})\chi(\mathbf{r}-\mathbf{b}) \tag{28}$$

$$V = \int_0^\infty d^2\mathbf{r}\hat{U}(\mathbf{r}+\mathbf{b}/2)\chi_a(\mathbf{r})\hat{U}(\mathbf{r}-\mathbf{b}/2) \tag{29}$$

$$\Pi = \int_0^\infty d^2\mathbf{r}\hat{U}^2(\mathbf{r}-\mathbf{b}/2)\chi_a(\mathbf{r}). \tag{30}$$

The relevant profiles $\psi(\mathbf{r})$ are used for the mirror coupling terms denoted by $\Upsilon^\dagger$, $\Lambda^\dagger$. Q, of order unity, is the eigenmode "confinement factor" within each cavity, and Υ, Λ, Π, $V \ll 1$ are the small inter-cavity coupling strengths. Analytic expressions for the coupling among fundamental mode profiles, using $U_{00}(\mathbf{r}) = \sqrt{2/\pi w^2}\exp(-r^2/w^2)$ inside (27, 28), are given in Appendix A (generalized for rectangular lattices with $b_x \neq b_y$). Defining the scale factor $\varepsilon \sim e^{-a^2/w^2} \sim e^{-b^2/w^2}$ we have the scaling

$$Q \sim 1 - \varepsilon^2 \gg \Pi \sim V \sim \varepsilon^{1/2} \gg \Upsilon \sim \varepsilon \gg \Lambda \sim \varepsilon^2. \tag{31}$$

Figure 6 shows contour plots of all coupling coefficients vs. b/w and b/a. A stand-out feature is that for weakly overlapping modes $b/w > 1$ the Υ coefficients become negative (shaded areas), despite the positive (Gaussian) eigenmode profiles U. The formal explanation lies in orthonormalization: the lattice-orthogonal $\hat{U}$, Figure 4, have negative tails for $r \geq b$, making the products $\hat{U}(r)\hat{U}(r-b)$ negative at the overlap regions $\chi(r) > 0$, Figure 5. The lattice-orthogonal coupling strengths (27, 28) are related to the earlier obtained [1] positive $\mathcal{Y}$ and Λ that employ unnormalized modes U instead of $\hat{U}$; these relations follow by substituting equation (8) as given in Appendix A. While Υ can be negative, Λ, V and Π remain positive.

A less straightforward approach, that offers more insight regarding the negative coupling values, is to retain the original (unhatted) eigenmodes in deriving the coupled cavity rate equations. Then equation (14) for the complex radiation amplitude assumes the form

$$\frac{\partial \mathcal{E}_{ij}}{\partial t} + \sum_{i'=i\pm1}\sum_{j'=j\pm1} C_{ij;i'j'}\frac{\partial \mathcal{E}_{i'j'}}{\partial t} = \frac{2\pi p^2}{\epsilon_o \hbar}\frac{\omega(\Gamma - i\Delta\omega)}{\Delta\omega^2+\Gamma^2}\zeta$$

$$\times\Bigg[\mathcal{Q}_{ij}\mathcal{N}_{ij}\mathcal{E}_{ij} + \sum_{i'=i\pm1}\sum_{j'=j\pm1}\Lambda_{ij;i'j'}\mathcal{N}_{i'j'}\mathcal{E}_{ij}$$

$$+\mathcal{Y}_{ij;i'j'}\left(\mathcal{N}_{ij}\mathcal{E}_{i'j'}+\mathcal{N}_{i'j'}\mathcal{E}_{i'j'}\right)\Bigg]+\cdots \qquad (32)$$

The right hand side contains the un-normalized coupling coefficients $\mathcal{Q}, \Lambda, \mathcal{Y}, \ldots$ In addition, there is coupling among the time derivatives on the left hand side, since the mode profiles are not lattice orthogonal. Thus, as the mode overlap stimulates gain on the rhs, the emitted radiation must be shared among all modes on the left. For large b/w the sharing "losses" into adjacent cavity modes exceed the gain benefit from induced cross-gain. It can be shown that diagonalizing the "tri-diagonal" left-hand side of (32), and regrouping the rhs using the coefficient relations (A.7), recovers equation (14) with the orthonormalized coefficients.

The coupling strengths, plotted in Figures 7a and 7b, depend primarily on the ratio of cavity center separation b to the $1/e^2$ mode waist w. For given b/w, there is a weaker dependence on the cavity separation to diameter ratio $b/2a$ (where $b/2a = 1$ corresponds to touching active areas and $b/2w = 1$ to touching mode waists). Note the trivial limit $\Lambda = \Upsilon = Q$ for zero separation $b = 0$ when all cavities coalesce into one.

Interestingly, the coupling goes to zero for uniform material properties, since equations (18, 17) revert to the orthonormality conditions (7) when $\chi_\alpha \equiv 1$ or $\psi \equiv 1$. Interactions "latch" on the variations $\chi(\mathbf{r})$ from a uniform "floor" value χ_o. Thus zero coupling values $\Lambda = \Upsilon = 0, (\Lambda^\dagger = \Upsilon^\dagger = 0)$ result both for zero gain (mirror) radius $\chi(\mathbf{r}) = 0$, and for infinite gain (mirror) radius $a, (a_m)$; in such cases $Q = 1, (Q_m = 1)$. Hence, individual cavities decouple gain-wise and reflection-wise when they share either an infinitely extending uniform gain or a common infinite mirror (but not both since that would lead to a single infinite cavity). We also have $\Pi, V = 0$ for a uniform absorption $\chi_\alpha = 1$, i.e., infinite a_α.

The evolution of the complex $\mathcal{E}_{ij} \equiv E_{ij}\exp[i\varphi_{ij}]$ is separated into amplitude and phase,

$$\frac{dE_{ij}}{dt} = \frac{1}{2E_{ij}}\left(\mathcal{E}^*_{ij}\frac{\partial \mathcal{E}_{ij}}{\partial t} + cc\right) \qquad (33)$$

$$\frac{d\varphi_{ij}}{dt} = \frac{1}{2iE^2_{ij}}\left(\mathcal{E}^*_{ij}\frac{\partial \mathcal{E}_{ij}}{\partial t} - cc\right). \qquad (34)$$

It is convenient at this point to introduce the rate equations in terms of the photon flux density $F \equiv P/\hbar\omega$ and the photon density $N_p = F/v_g$, where $P = v_g\epsilon_o EE^*/8\pi$ is the power and v_g is the group velocity. Converting the microscopic quantities in equations (33, 34) into phenomenological macroscopic gain coefficients $g_r + ig_i$ where $g_r = g_o \ln[N_{ij}/N_{tr}]$, $g_i = \iota g_r$, N is the total (resonant plus nonresonant) over equilibrium carrier density, and the parameters g_o and N_{tr} are given in terms of the material properties and temperature T, yields [1], retaining only the nearest interactions $i' = i \pm 1, j' = j \pm 1$

$$\frac{dN_{ij}}{dt} = \frac{J_{ij}}{ed_w} - \gamma N_{ij} - BN^2_{ij} - g_r \ln \hat{N}_{ij}F_{ij}$$

$$- g_r \ln \hat{N}_{ij}\Lambda \sum_{i'=i\pm1}\sum_{j'=j\pm1} F_{i'j'} - g_r \ln \hat{N}_{ij}\Upsilon$$

$$\times \sum_{i'=i\pm1}\sum_{j'=j\pm1} 2\sqrt{F_{ij}F_{i'j'}}\cos\left[\varphi_{ij}-\varphi_{i'j'}\right] \qquad (35)$$

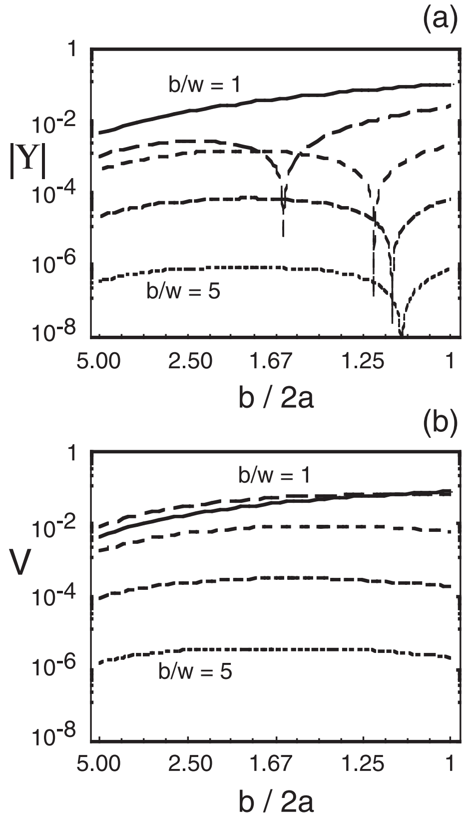

Fig. 7. Linear plots of coupling coefficient strength along vertical lines of given $b/w = 1, 2, 3, 4, 5$ in Figure 6. (a) Absolute value of Υ vs. decreasing cavity separation $b/2a$. Dips mark $\Upsilon = 0$ with negative values to the left. (b) V vs. decreasing cavity separation $b/2a$ (positive). Coupling strength is more sensitive to cavity separation relative to mode waist b/w, top to bottom curves, than cavity separation relative to gain area size, left to right.

$$
\begin{aligned}
\frac{dF_{ij}}{dt} &= v_g \zeta g_r \ln \hat{N}_{ij} F_{ij} - v_g \mu F_{ij} \\
&+ \sum_{i'=i\pm1} \sum_{j'=j\pm1} \left(\varLambda v_g \zeta g_r \ln \hat{N}_{i'j'} + \varLambda^{\dagger} v_g \mu - \varPi v_g \delta\hat{\alpha} \right) F_{ij} \\
&+ \varUpsilon \sum_{i'=i\pm1} \sum_{j'=j\pm1} v_g \zeta \hat{g} \left[\ln \hat{N}_{ij} + \ln \hat{N}_{i'j'} \right] \\
&\qquad \times \sqrt{F_{ij} F_{i'j'}} \cos \left[\varphi_{ij} - \varphi_{i'j'} + \vartheta \right] \\
&- V \sum_{i'=i\pm1} \sum_{j'=j\pm1} 2 v_g \delta\hat{\alpha} \sqrt{F_{ij} F_{i'j'}} \cos \left[\varphi_{ij} - \varphi_{i'j'} \right] \\
&+ \varUpsilon^{\dagger} \sum_{i'=i\pm1} \sum_{j'=j\pm1} 2 v_g \mu \sqrt{F_{ij} F_{i'j'}} \cos \left[\varphi_{ij} - \varphi_{i'j'} \right] \\
&- \varUpsilon \sum_{i'=i\pm1} \sum_{j'=j\pm1} 2 \omega \delta\hat{\epsilon} \sqrt{F_{ij} F_{i'j'}} \sin \left[\varphi_{ij} - \varphi_{i'j'} \right]
\end{aligned}
\qquad (36)
$$

$$
\begin{aligned}
\frac{d\varphi_{ij}}{dt} &= v_g \zeta \frac{g_i}{2} \ln \hat{N}_{ij} \\
&+ \varLambda \sum_{i'=i\pm1} \sum_{j'=j\pm1} \left(v_g \zeta \frac{g_i}{2} \ln \hat{N}_{i'j'} + \omega \frac{\delta\hat{\epsilon}}{2} \right) \\
&+ \varUpsilon \sum_{i'=i\pm1} \sum_{j'=j\pm1} v_g \zeta \frac{\hat{g}}{2} \left[\ln \hat{N}_{ij} + \ln \hat{N}_{i'j'} \right] \\
&\qquad \times \sqrt{\frac{F_{i'j'}}{F_{ij}}} \sin \left[\varphi_{ij} - \varphi_{i'j'} + \vartheta \right] \\
&- V \sum_{i'=i\pm1} \sum_{j'=j\pm1} 2 v_g \frac{\delta\hat{\alpha}}{2} \sqrt{\frac{F_{i'j'}}{F_{ij}}} \sin \left[\varphi_{ij} - \varphi_{i'j'} \right] \\
&+ \varUpsilon^{\dagger} \sum_{i'=i\pm1} \sum_{j'=j\pm1} 2 v_g \frac{\mu}{2} \sqrt{\frac{F_{i'j'}}{F_{ij}}} \sin \left[\varphi_{ij} - \varphi_{i'j'} \right] \\
&+ \varUpsilon \sum_{i'=i\pm1} \sum_{j'=j\pm1} 2 \omega \frac{\delta\hat{\epsilon}}{2} \sqrt{\frac{F_{i'j'}}{F_{ij}}} \cos \left[\varphi_{ij} - \varphi_{i'j'} \right].
\end{aligned}
\qquad (37)
$$

Above we have defined $\hat{N}_{ij} \equiv N_{ij}/N_{tr}$ with N_{tr} the transparency density. We have also combined the real and imaginary gain contributions using $g_r = \hat{g} \cos\vartheta$, $g_i = \hat{g} \sin\vartheta$ with $\hat{g} \equiv \sqrt{g_r^2 + g_i^2}$, $\vartheta \equiv \tan^{-1} g_i/g_r = \tan^{-1}\iota$.

4 Relaxation to Bloch eigenstates

The collective array behavior is investigated via numerical integration of the coupled lattice equations (35–37). Constant in time drive currents, equal for all cavities, $J_{ij}(\mathbf{r}) = J_o \chi(r)$ are turned on at $t = 0$. Random initial conditions are used for the carrier density, the radiation intensity and phase in each cavity. A spontaneous relaxation to collective steady states usually occurs within a short period. Typical example is shown in Figure 8. Collective modes, such as Figures 9a and 9b, exhibit constant radiation intensity and density in each cavity, $F_{ij} = F_o, N_{ij} = N_o$, and a constant in time, uniform in space phase difference among lattice sites $\varDelta\varphi_i \equiv \varphi_i - \varphi_{i-1} = \varDelta\varphi_o$, manifesting spontaneous cavity phase locking. The time lapsed to phase lock depends on the coupling strength, and is shorter for higher $\varUpsilon$.

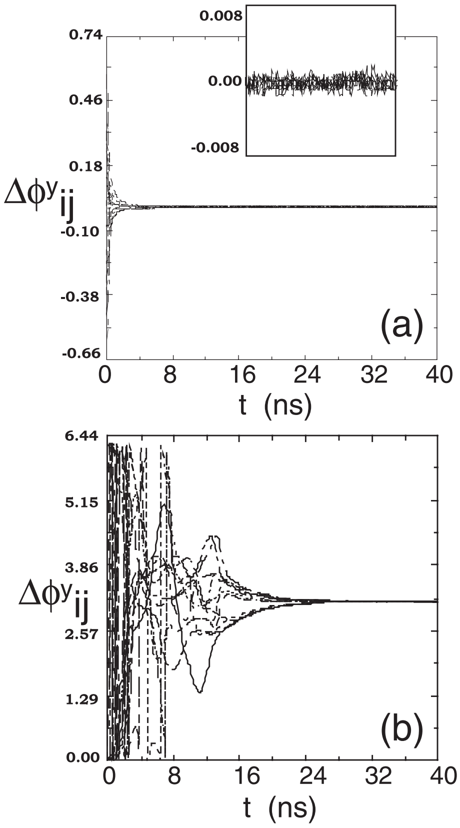

Fig. 8. Spontaneous phase lock in a 2-D 8×8 periodic array from uniformly distributed random initial conditions and for constant bias current $I \simeq 3.13 I_{th}$ (a). Phase difference among adjacent cavities in the y-direction for (a) in-phase locking for coupling strength $Y = 0.006$. (b) Out-of-phase locking for coupling strength $Y = -0.006$. The inset in (a) shows the spontaneous phase fluctuations on expanded vertical scale.

The structure of collective eigenstates is analytically obtained from the zeros of equations (35, 36). Since only phase differences enter the dynamic equations for the density (35) and the intensity (36) what matters is the phase difference evolution, obtained by subtracting equations (37) among any two neighboring sites for $\varDelta^x \varphi^{\pm}_{i,j} \equiv \varphi_{i,j} - \varphi_{i\mp1,j}$ and $\varDelta^y \varphi^{\pm}_{i,j} \equiv \varphi_{i,j} - \varphi_{i,j\mp1}$. Because of lattice periodicity $\varDelta^x \varphi^{\pm}_{i,j}$ and $\varDelta^y \varphi^{\pm}_{i,j}$ are related through the Bloch condition thus it is sufficient to record

$\Delta^y\varphi^-_{i,j}$, given by

$$
\begin{aligned}
\frac{d\Delta\varphi_{ij}}{dt} &= v_g\zeta\frac{g_i}{2}\ln\left(\frac{N_{ij}}{N_{i,j-1}}\right)\\
&+\Lambda\sum_{i'=i\pm1}\sum_{j'=j\pm1} v_g\zeta\frac{g_i}{2}\ln\left(\frac{N_{i'j'}}{N_{i',j'-1}}\right)\\
&+\Upsilon\sum_{i'=i\pm1}\sum_{j'=j\pm1} v_g\zeta\frac{\hat{g}}{2}\left\{\ln\left(\frac{N_{ij}N_{i'j'}}{N_{tr}^2}\right)\right.\\
&\qquad\times\sqrt{\frac{F_{i'j'}}{F_{ij}}}\sin[\Delta\varphi^{\pm}_{ij}+\vartheta]\\
&\left.-\ln\left(\frac{N_{i,j-1}N_{i',j'-1}}{N_{tr}^2}\right)\sqrt{\frac{F_{i'j'-1}}{F_{i,j-1}}}\sin[\Delta\varphi^{\pm}_{i,j-1}+\vartheta]\right\}\\
&-V\sum_{i'=i\pm1}\sum_{j'=j\pm1} 2v_g\frac{\delta\hat{\alpha}}{2}\left\{\sqrt{\frac{F_{i'j'}}{F_{ij}}}\sin\Delta\varphi^{\pm}_{ij}\right.\\
&\qquad\left.-\sqrt{\frac{F_{i'j'-1}}{F_{i,j-1}}}\sin\Delta\varphi^{\pm}_{i,j-1}\right\}\\
&+\Upsilon^{\dagger}\sum_{i'=i\pm1}\sum_{j'=j\pm1} 2v_g\frac{\mu}{2}\left\{\sqrt{\frac{F_{i'j'}}{F_{ij}}}\sin\Delta\varphi^{\pm}_{ij}\right.\\
&\qquad\left.-\sqrt{\frac{F_{i'j'-1}}{F_{i,j-1}}}\sin\Delta\varphi^{\pm}_{i,j-1}\right\}\\
&+\Upsilon\sum_{i'=i\pm1}\sum_{j'=j\pm1} 2\omega\frac{\delta\hat{\epsilon}}{2}\left\{\sqrt{\frac{F_{i'j'}}{F_{ij}}}\cos\Delta\varphi^{\pm}_{ij}\right.\\
&\qquad\left.-\sqrt{\frac{F_{i'j'-1}}{F_{i,j-1}}}\cos\Delta\varphi^{\pm}_{i,j-1}\right\}. \qquad (38)
\end{aligned}
$$

It is not the individual cavity phases φ_{ij}, but their differences that "freeze" in time $d\Delta\varphi_{ij}/dt = 0$. Hence, phase "crystallization" among cavity radiation envelopes parallels phase crystallization among atomic wavefunctions in lattices.

Of the most general set of steady states, yielding a zero right hand side in equations (35, 36, 38), we are interested in the uniform solutions subset, with constant density and amplitude over the array given respectively by $N_{ij} = N_o$ and $F_{ij} = F_o$. Inspection shows that *any* uniform phase difference between adjacent sites $\overset{x}{\Delta\varphi}_{ij} = \overset{x}{\Delta\varphi}_o$, $\overset{y}{\Delta\varphi}_{ij} = \overset{y}{\Delta\varphi}_o$ yields such a steady-state. Periodic boundaries every M and N sites, and and the uniformity of $\Delta\varphi$ among sites lead to $\overset{x}{\Delta\varphi}_o = m(2\pi)/M = \mathbf{K}^{mn}\cdot\mathbf{b}_x$ and $\overset{y}{\Delta\varphi}_o = n(2\pi)/N = \mathbf{K}^{mn}\cdot\mathbf{b}_y$, where $\mathbf{K}^{mn} \equiv (K_m, K_n) = (m2\pi/Mb_x, n2\pi/Nb_y)$ is a wavevector of the inverse lattice. A given steady-state will henceforth be labeled by the corresponding Brillouin zone vector $\mathbf{K}^{mn}$. The phase at the ijth site is linear in lattice coordinates, $\varphi_{ij} = i\overset{x}{\Delta\varphi}_o + j\overset{y}{\Delta\varphi}_o = (i\mathbf{b}_x + j\mathbf{b}_y)\cdot\mathbf{K}^{mn} = \mathbf{K}^{mn}\cdot\mathbf{R}_{ij}$ (within an arbitrary constant.) Substituting the values $\mathcal{E}_{ij} = E_o e^{i\phi_{ij}}$ (where $E_o \propto \sqrt{F_o}$) in the electric field expansion, and factoring out the common fast-phase dependence $e^{i(kz-\omega_o t)}$ yields the mn-eigenmode envelope over the array

$$\mathbf{E}^{mn}(\mathbf{r}) = \sum_{i,j} E_o e^{i\mathbf{K}^{mn}\cdot\mathbf{R}_{ij}}U(\mathbf{r}-\mathbf{R}_{ij}). \qquad (39)$$

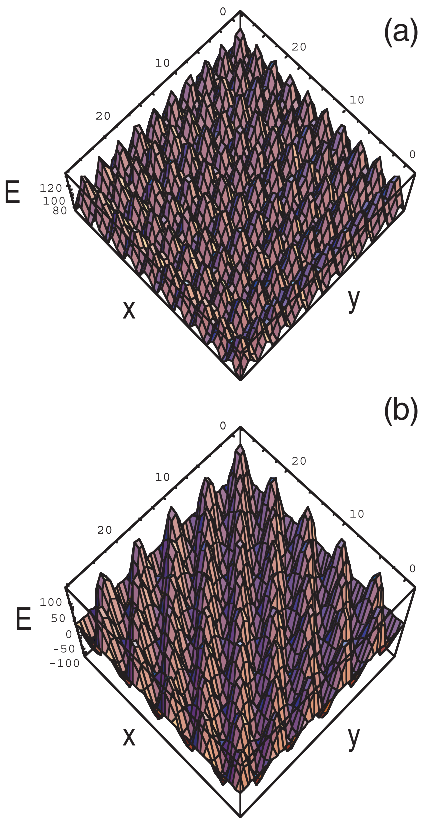

Fig. 9. Snapshot of the radiation field, superposition of all cavity fields, (a.u) over a 9×9 periodic array at $t = 40$ ns. (a) In-phase locked steady-state for positive coupling constant $G = 0.006$. (b) Anti-phase locked steady-state for negative coupling constant $G = -0.006$. Lattice separation is twice the cavity mode waist $b/w = 2$, with $b_x = b_y = 3$ (a.u).

Bloch eigenstates thus emerge naturally as the lattice steady-states from the dynamic lattice equations. They are formally equivalent to stationary perturbation theory results involving cavity mode superpositions with expansion coefficients $C_{ij}(K^{mn}) = E_o e^{i\mathbf{K}^{mn}\cdot\mathbf{R}_{ij}}$

Similar general conclusions have been described before using a model with gain coupling only [1]. Here we will discuss (a) the effects of the added mirror interference and passive dielectric, as well as absorption coupling, on the eigenmode structure (b) how the overall coupling strength determines phase selection, particularly in- vs. anti-phasing (c) the departures from Bloch states caused by finite array boundaries.

4.1 Eigenmode effects

While the steady-state phase does not depend explicitly on the cavity interaction details, the steady state amplitudes and densities depend on both $\Delta\varphi^{mn}$ and the various interaction coupling strengths, $F_o = F(K^{mn}; \Upsilon, V, \ldots)$, $N_o = F(K^{mn}; \Upsilon, V, \ldots)$. They are analytically obtained from the zeros of the rhs of equation (35, 36). Substituting $\Delta\varphi^{mn}$, and observing that the sinusoidal terms cancel out at steady-state due to $\Delta\varphi_{i,i+1} = -\Delta\varphi_{i,i-1}$ etc., yields

$$\begin{aligned} 0 &= \frac{J_{ij}}{ed_w} - \gamma N_o - BN_o^2 - g_0 \ln \hat{N}_o F_o - 4g_r \ln \hat{N}_o \Lambda F_o \\ &\quad - 4\Upsilon g_r \ln \hat{N}_o F_o (\cos\Delta\varphi_m + \cos\Delta\varphi_n) \qquad (40) \\ 0 &= v_g \zeta g_r \ln \hat{N}_o F_o - v_g \mu F_o \\ &\quad + 4v_g \left(\Lambda \zeta g_r \ln \hat{N}_o - \Pi \delta\hat{\alpha} + \Lambda^\dagger \mu\right) F_o \\ &\quad + 4v_g \left(\Upsilon \zeta g_r \ln \hat{N}_o - V \delta\hat{\alpha} + \Upsilon^\dagger \mu\right) \\ &\quad \times F_o (\cos\Delta\overset{x}{\varphi}_m + \cos\Delta\overset{y}{\varphi}_n). \qquad (41) \end{aligned}$$

It is obvious from (40, 41) that passive dielectric coupling $\delta\epsilon$ does not affect N_o and F_o. Dielectric coupling enters in the individual cavity phase advance equation (37). At steady-state it causes a systematic frequency shift for all cavities

$$\Delta\omega_\epsilon = \frac{\omega}{2}\delta\hat{\epsilon}\left[4\Lambda + 4\Upsilon(\cos\Delta\overset{x}{\varphi}_m + \cos\Delta\overset{y}{\varphi}_n)\right], \qquad (42)$$

which can be absorbed from the start into the cavity frequency, and does not affect $\Delta\varphi$. The resulting from (40, 41) steady-state amplitudes and densities values are

$$N_o^{mn} = N_{tr} \exp\left[\frac{\mu}{\zeta g_r} \Xi(\mathbf{K}^{mn})\right] \qquad (43)$$

$$F_o^{mn} = \zeta \frac{\gamma}{\mu} \left\{ \frac{J_o}{ed_w \gamma} - \frac{\tilde{\gamma}}{\gamma} N_{tr} \exp\left[\frac{\mu}{\zeta g_r} \Xi(\mathbf{K}^{mn})\right] \right\} \qquad (44)$$

where the coupling effect is embodied in the lattice factor $\Xi^{mn} \equiv \Xi(\mathbf{K}^{mn})$, defined as

$$\begin{aligned} &\Xi^{mn} \equiv \\ &\frac{1 - 4\Lambda^\dagger - 4\Upsilon^\dagger(\cos\Delta\overset{x}{\varphi}_m + \cos\Delta\overset{y}{\varphi}_n)}{1 + 4(\Lambda - \Pi\delta\hat{\alpha}/\mu) + 4(\Upsilon - V\delta\hat{\alpha}/\mu)(\cos\Delta\overset{x}{\varphi}_m + \cos\Delta\overset{y}{\varphi}_n)} \\ &\quad \simeq 1 - 4(\Lambda^\dagger + \Lambda - \Pi\delta\hat{\alpha}/\mu) \\ &\qquad - 4(\Upsilon^\dagger + \Upsilon - V\delta\hat{\alpha}/\mu)(\cos\Delta\overset{x}{\varphi}_m + \cos\Delta\overset{y}{\varphi}_n). \qquad (45) \end{aligned}$$

Thus mirror interference coupling $Y^\dagger$ and passive intercavity absorption V affect the mode structure to the same order as gain coupling Υ. We have neglected quadratic terms in the coupling constants, thus using $\zeta g_r \ln \hat{N}_o \simeq \mu$ at steady-state. The isolated cavity steady-state values $N_o = N_{tr} \exp[\mu/\zeta g_r]$, $F_o = \zeta/\mu\,[J_o/ed_w - \tilde{\gamma} N_o]$ are recovered in the uncoupled limit $\Upsilon^\dagger$, $\Lambda^\dagger$, Υ, Λ, V, $\Pi = 0$ when $\Xi \to 1$. The steady-state density (43) is also expressed as $N_o^{mn} = (N_o)^{\Xi_{mn}}$.

4.2 Phase selection

The stability analysis of Section 5 will show that for values $g_i/g_r \leq 1$ half of the steady-state values $(\Delta\overset{x}{\varphi}_m, \Delta\overset{y}{\varphi}_n)$ are stable against small perturbations. Yet, our numerical simulations show that, starting from arbitrary initial conditions, the lattice settles to either in-phased $(\Delta\overset{x,y}{\varphi}_o = 0)$ or anti-phased $(\Delta\overset{x,y}{\varphi}_o = \pi)$ array configuration. To understand the in- vs. out-of-phase preference we notice that, during the final approach towards steady-state $\mathrm{mod}(\Delta\varphi_{ij}, \pi) \simeq 0$, the $\sin\Delta\varphi_{ij} \simeq 0$ terms are negligible and the radiation amplitude and phase equations are simplified as

$$\begin{aligned} \frac{F_{ij}}{dt} &= v_g \zeta g_r \ln \hat{N}_{ij} F_{ij} - v_g \mu F_{ij} \\ &\quad + \sum_{i'=i\pm1} \sum_{j'=j\pm1} 2v_g \mathcal{G}_{ij,i'j'} \sqrt{F_{ij} F_{i'j'}} \cos\Delta\varphi_{ij,i'j'} \\ &\quad + \sum_{i'=i\pm1} \sum_{j'=j\pm1} \left(\Lambda v_g \zeta g_r \ln \hat{N}_{i'j'} + \Lambda^\dagger v_g \mu - \Pi v_g \delta\hat{\alpha}\right) F_{ij} \end{aligned} \qquad (46)$$

$$\begin{aligned} \frac{d\Delta\varphi_{ij}}{dt} &= v_g \zeta \frac{g_i}{2} \ln\left(\frac{N_{ij}}{N_{i,j-1}}\right) \\ &\quad + \Lambda \sum_{i'=i\pm1} \sum_{j'=j\pm1} v_g \zeta \frac{g_i}{2} \ln\left(\frac{N_{i'j'}}{N_{i',j'-1}}\right) \\ &\quad + \sum_{i'=i\pm1} \sum_{j'=j\pm1} v_g 2 \left\{ \mathcal{G}_{ij,i'j'} \sqrt{\frac{F_{ij}}{F_{i'j'}}} \sin\Delta\varphi_{ij,i'j'} \right. \\ &\quad \left. - \mathcal{G}_{ij-1,i'j'-1} \sqrt{\frac{F_{ij-1}}{F_{i'j'-1}}} \sin\Delta\varphi_{ij-1,i'j'-1} \right\} \qquad (47) \end{aligned}$$

where the various phase-dependent coupling contributions are combined inside the factor

$$\mathcal{G}_{ij,i'j'} = \Upsilon \zeta \hat{g} \frac{1}{2} \ln\left(\hat{N}_{ij} \hat{N}_{i'j'}\right) - V\delta\hat{\alpha} + \Upsilon^\dagger \mu \qquad (48)$$

Given that near steady-state $\hat{N}_{ij} \simeq N_o + \mathcal{O}(\Upsilon)$, $\hat{F}_{ij} \simeq F_o + \mathcal{O}(\Upsilon)$, the overall effect of the coupling interactions on the growth rate is given, to first order in coupling strengths, by

$$\left.\frac{1}{F_{ij}} \frac{dF_{ij}}{dt}\right|_{cpl} \simeq 8v_g G_o \cos\Delta\varphi_o + \mathcal{O}(\Upsilon^2) \qquad (49)$$

where $G_o = \Upsilon \zeta \hat{g} \ln \hat{N}_o - V\delta\hat{\alpha} + \Upsilon^\dagger \mu$. Our numerical observations are consistent with *gain maximization*: the phase selection is such that the overall coupling effects enhance the growth rate (i.e. “gain”). Maximum $G_o \cos\Delta\varphi_o$ implies $\Delta\varphi_o = 0$ for $G_o > 0$ and $\Delta\varphi_o = \pi$ for $G_o < 0$. Thus it is the combined coupling strength from mirror interference, absorption coupling and gain coupling that determines phase via the G_o sign. The real dielectric (i.e. index) interference $\Delta\epsilon$ does not enter G_o and phase selection.

Most of the usual cavity arrangements [13–17] correspond to $G_o < 0$ causing anti-phased arrays. That happens because, for site separation larger than the mode waist $b/w > 2$ the gain and mirror coupling coefficients are negative $\Upsilon, \Upsilon^\dagger < 0$, while inter-cavity absorption coupling remains positive $V > 0$ over the entire parameter range. The cases of an infinite extent shared mirror (zero mirror interferences $\Upsilon^\dagger \to 0_-$), or infinite extent shared gain region (zero gain cross-coupling $\Upsilon \to 0_-$) also fall into that category. To achieve $G_o > 0$ for an in-phase array one must have $\Upsilon\mu + \Upsilon^\dagger\mu > V\delta\hat{\alpha}$. One approach is reducing passive absorption between cavities, making $\delta\alpha < 0$. Increasing the DBR reflectivity *between* cavities $R_1 - R_o > 0$ also makes $\Upsilon^\dagger$ positive for Υ negative, according to definition after (24). Closely packing the cavities $b/w < 2$ so that $\Upsilon, \Upsilon^\dagger$ turn positive, is also an alternative; then, because of the scaling (31), the absorption must be uniformly distributed, so that $V \to 0_+$.

Next figures show typical lattice simulation results, in the unconditionally stable regime. Figures 8a and 8b show the dynamical evolution of the phase difference $\Delta\phi^y_{ij}$ for 9×9 arrays with periodic boundary conditions. The cavity parameters are $\mu = 1347$ cm^{-1}, $g_r = 1117$ cm^{-1}, $\gamma = 2 \times 10^9$ s^{-1}, $B = 3 \times 10^{-11}$ s^{-1}cm^3, $d_w = 30$ nm and current $I = 3.13 I_{th} = 6.09$ mA over active radius $a = 3$ μm and a ratio $g_i/g_r = 0.5$. Random initial conditions with subthreshold density are used. Spontaneous emission is always superimposed on the rate equations [19], via a numerical implementation of random photon emissions. Figure 8a shows that spontaneous in-phase locking with $\Delta\overset{x}{\varphi}_o = \Delta\overset{y}{\varphi}_o = 0$ occurs for coupling strength $G_o = 0.006$. Phase locking is not impeded by the ever-present spontaneous phase noise, (magnified insert Fig. 8a). The envelope of the electric field over the array at $t = 20$ ns is shown in Figure 9a. Changing the coupling strength sign to negative $G_o = -0.006$ leads to an anti-phased array steady-state $\Delta\overset{x}{\varphi}_o = \Delta\overset{y}{\varphi}_o = \pi$, with the field envelope plotted in Figure 9b. The corresponding dynamic phase evolution is shown in 8b. It appears that steady-state phase selection according to maximum gain configuration is of probabilistic nature; for random initial conditions the odds for 0 or π phasing are overwhelming. A rare occasion where $\Delta\overset{y}{\varphi}_o \neq \Delta\overset{x}{\varphi}_o$ with π-phasing in y and $3\pi/4$-phasing in x, is shown in Figure 10, for the same parameters as Figure 9b.

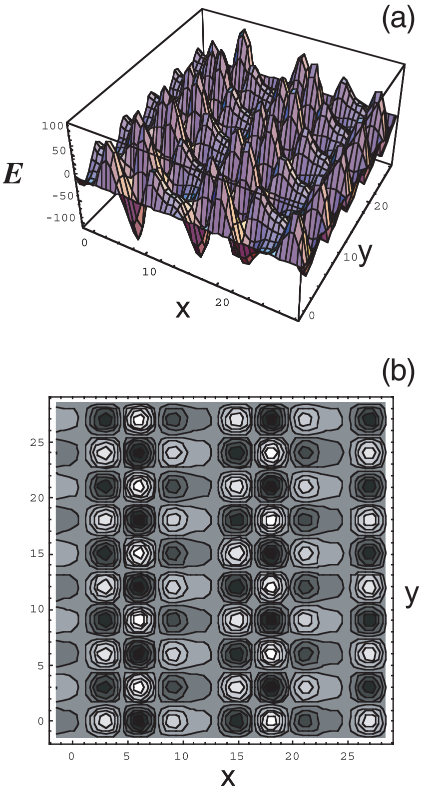

Fig. 10. Snapshot of the radiation amplitude profile (a.u) over a 9×9 periodic array array at $t = 40$ ns. Anti-phase locking with different $(x - y)$-phase pitch $\Delta\Phi_x = 3\pi/4$ and $\Delta\Phi_y = \pi$, for the same parameters as Figure 6b. (a) 3-D radiation field, superposition of all cavity fields. (b) Contour plot of above. Lattice separation is twice the cavity mode waist $b/w = 2$, with $b_x = b_y = 3$ (a.u).

4.3 Finite array boundaries

Boundaries in finite size arrays can cause deviations from Bloch eigenstates due to edge effects and boundary layer generation. Finite boundaries are implemented by removing the appropriate coupling terms at the edge sites. Figures 11 show the final steady-state from simulations of a 9×9 array. Nearly in-phase locking results for $G_o = 0.006 > 0$ and identical other parameters as before. Here however the phase difference among sites is not uniform but varies in space: Figure 11a shows a linear variation of $\Delta\overset{x}{\varphi}_i$ along x (same holds for $\Delta\overset{y}{\varphi}_j$ along y.) Instead of uniform (Bloch) phase difference $\Delta\varphi^x_i = 0$ we have uniform gradient $d\Delta\overset{x}{\varphi}/dx = d\Delta\overset{y}{\varphi}/dy$ equivalent to a constant second derivative $\nabla^2\varphi = \text{const} \neq 0$. Figure 11b shows boundary layer formation: the peak cavity field E_{ij} varies near the boundaries instead of $E_{ij} = E_o$ everywhere. The plot of the radiation field envelope is shown in Figure 11c. The boundary layer in the cavity densities is shown in Figure 11d. Simulations with negative $G_o = -0.006 < 0$ led to (nearly) anti-phased steady-states with similar boundary layers and linear phase gradients around $\Delta\varphi = \pi$.

Boundary layers are a consequence of the coupling nonlinearity. In linearly-coupled arrays, boundary conditions are enforced by phase selection alone. For example, a 1-D N-size array settles into a standing Bloch wave of the form $A_j = A\sin j\Delta\varphi_k$, $\Delta\varphi_k = [k\pi/(N+1)]$ $(k \neq 0, N+1)$; the values $j = 0$, $j = N+1$ represent fictitious "outer sites" of permanent zero "displacement" $A_0 = A_{N+1} = 0$ so that they exert no force on the end-sites $j = 1$, $j = N$. Nonlinear coupled arrays posses the extra ability to adjust end-cavity frequencies (i.e. non-linear spring constants) by adjusting steady-state intensity at boundary sites. It allows a non-Bloch state of uniform phasing and edge-varying amplitude $A_j = A(j)\cos[j0]$ (in-phase) or $A_j = A(j)\cos[j\pi]$ (anti-phase). Incidentally, the phase difference for linear

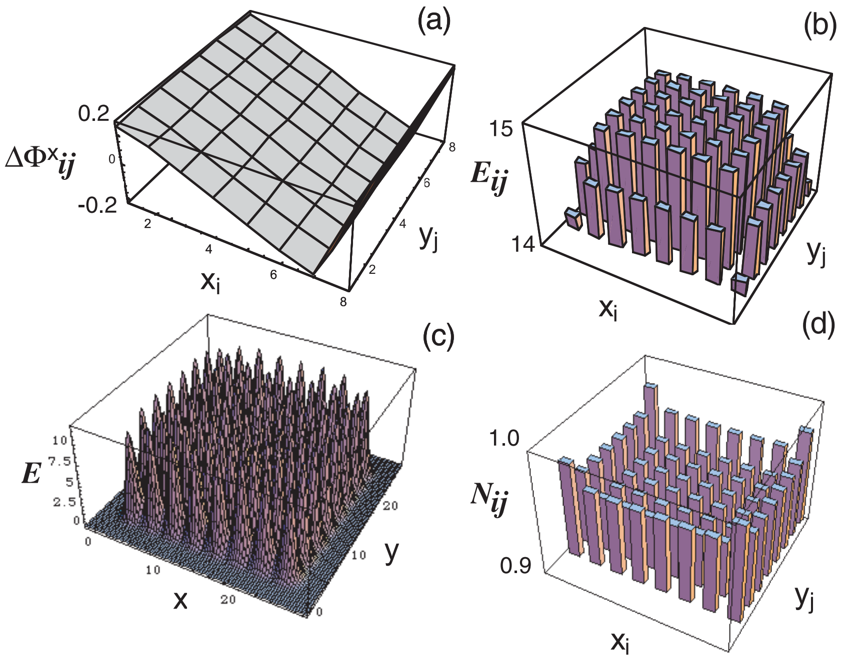

Fig. 11. Snapshot of the radiation profiles (a.u) over a 8×8 finite array array at $t = 40$ ns, for the same parameters as Figure 8a. Phase difference (x-direction) among neighbor sites over lattice, (b) distribution of peak field E_{ij} (a.u.) in each lattice cavity shows boundary layer formation, (c) 3-D radiation field shows in-phase locking, (d) carrier density N_{ij}/N_{th} in each cavity.

coupled arrays cannot be exactly zero or π, yielding a sinusoidal rather than a flat array intensity profile inside the array.

5 Phase stability and lattice oscillations

Further understanding of the array behavior results by analyzing the stability of small oscillations around the steady state. Here we assume that a steady state $\Delta\varphi_{ij} = \Delta\varphi_o$, $\mathcal{E}_{ij} = \mathcal{E}_o$, $N_{ij} = N_o$ has been reached and examine the evolution of small perturbations about these values. Collective modes over a periodic lattice must also be of the Bloch wave form

$$\delta A = \delta A_o e^{\lambda t} \sum_{i,j} e^{\kappa \cdot \mathbf{R}_{ij}} \tag{50}$$

where δA reflects either density or radiation amplitude. Note that equation (50) is the discretized version of the continuous Bloch function $\delta A_o(x) e^{i\kappa x}$ where the lattice-periodic envelope is sampled at the lattice sites $\delta A_o(x = 0) = \delta A_o(x = b_x) = \cdots = \delta A_o(x = jb_x)$. Replacing independent phase variations by a lattice-periodic phase perturbation manifests the transition to collective behavior with long range coherence (far from steady state, the site phases φ_{ij} are treated as independent variables, following equations (37, 38). The description resembles the dynamic behavior of a periodic, spring-coupled mass system, a model finding wide applications in lattice dynamics. Due to the periodicity, linearization of (35, 37) about any site leads to identical stability equations. The polar diagram Figure 12 shows electric field perturbations both in and out of phase ($\delta E_\perp, \delta E_\parallel$), relative to the steady-state field "direction" at each site. Picking an arbitrary site as reference, $E_{ij} \equiv E_o$, $\varphi_{ij} = 0$ the neighboring site perturbations are related by $\delta \mathbf{E}_{i\pm 1} = \delta E_o(\cos\kappa b_x, \pm\sin\kappa b_x)$ (and similar for $\delta \mathbf{E}_{j\pm 1}$). The site phase changes by $\delta\varphi_\pm \cong \pm\sin^{-1}(\delta E_\perp/E_o) \simeq \pm(\delta E_o/E_o)\sin\kappa b_x$. Since the x-coordinate can be thought of as a continuously running site index i, we have $\Delta\varphi_{i,i-1} \simeq b_x(d\varphi_i/dx)$ (and

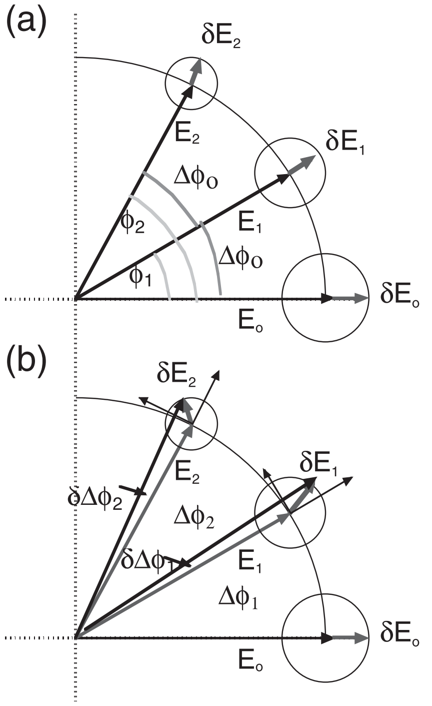

Fig. 12. Polar plane representation of the lattice amplitude and phase perturbations along adjacent sites E_o, E_1, E_2... (a) sinusoidal changes in electric field strength only without changing the relative phase between lattice sites, (b) sinusoidal changes in both electric field strength and the relative phase between lattice sites.

similar along y). Hence, analytic continuity in the definition of the phase difference among sites requires that $\delta(\Delta\varphi)_x \propto d(\delta\varphi_i)/dx = \delta\Phi_o \cos\kappa_x b_x$ where $\delta\Phi_o = \delta E_o/E_o = \delta F_o/2F_o$. Picking an arbitrary $\mathbf{R}_{ij} = \mathbf{R}_o$, expanding around equilibrium and use of (50) yields the following equation for perturbations about steady-state

$$\frac{d}{dt}\begin{pmatrix}\delta N_o\\ \delta F_o\\ \delta\Phi_o\end{pmatrix} = \begin{pmatrix} D_{NN} & D_{NF} & D_{N\Phi}\\ D_{FN} & D_{FF} & D_{N\Phi}\\ D_{\Phi N} & D_{\Phi F} & D_{\Phi\Phi}\end{pmatrix}\begin{pmatrix}\delta N_o\\ \delta F_o\\ \delta\Phi_o\end{pmatrix} = \lambda\begin{pmatrix}\delta N_o\\ \delta F_o\\ \delta\Phi_o\end{pmatrix}. \tag{51}$$

The elements $D_{XY} \equiv \partial(\dot{X})/\partial Y$ with X, Y being either of N, $\mathcal{E}$, $\Delta\varphi$ are found from the rhs of (35, 37) at steady-state, (Appendix B). It is instructive to consider certain limiting cases before a full diagonalization is attempted.

Consider first the limit where only in-phase variations is allowed in the electric field, $\delta F_\perp = \delta\varphi = 0$. While amplitude and density vary sinusoidally over space (and time), the phase difference among adjacent sites maintains its equilibrium value, hence $D_{N\Phi} = D_{F\Phi} = D_{\Phi\Phi} \equiv 0$. Diagonalization of (51) in this limit factors out to one trivial eigenvalue $\lambda_3 = 0$ and two eigenvalues $\lambda_{1,2}$ from the upper 2×2 submatrix determinant

$$\lambda^2 - (D_{NN}+D_{FF})\lambda + (D_{NN}D_{FF} - D_{NF}D_{FN}) = 0. \tag{52}$$

Letting $\Theta = \lambda_{1,2}$ yields the dispersion relation for collective modes over the cavity lattice,

$$\Theta(\kappa';K) = \Gamma(\kappa';K) \pm i\Omega(\kappa';K)\sqrt{1 - \frac{\Gamma^2(\kappa';K)}{\Omega^2(\kappa';K)}} \tag{53}$$

where $\Omega \equiv \sqrt{D_{NF}|D_{FN}| - D_{FF}D_{NN}}$ and $\Gamma \equiv (D_{NN} + D_{FF})/2$. The two dispersion branches form the propagating bands of an active photonic lattice. Using the steady state values in the rhs of (53), the frequency and the decay rates are respectively given by

$$\Omega(\kappa;K) = \hat{\Omega}(K) \times \left\{1 - \frac{v_g\mu\Gamma_o}{\Omega_o^2} 2G_o \frac{\cos K_m b(1-\cos\kappa_x b) + (x\to y)}{Z(\kappa;K)}\right\}^{1/2}, \tag{54}$$

$$\Gamma(\kappa;K) = -|\Gamma_o| - \gamma_s\left[Z(\kappa;K) - 1\right] - v_g\mu 2G_o \times \left[\cos K_{mb}(1-\cos\kappa_x b) + (x\to y)\right] \tag{55}$$

with $Z(\kappa;K) = 1 + 2\Lambda\cos\kappa_x b + 4Y\cos K_m b + (x\to y)$. A perturbation of wavenumber $\boldsymbol{\kappa}$ relative to the lattice phase involves free-space wavenumbers $\boldsymbol{\kappa}'_\pm = K \pm \kappa$ through lattice period coupling, contained in $\cos K_m b \cos\kappa_x b$ terms. The coupled cavity frequency scales as $\hat{\Omega} = \Omega_o\sqrt{Z(\kappa;K)}$ where Ω_o is the oscillation (relaxation) frequency for an isolated cavity. The decay rate Γ is related to the stimulated $\gamma_s = g_oF_o/N_o$ and the total non-stimulated $\tilde{\gamma} = \gamma + 2BN_o$ decay rates. In the $G_o = 0$, $Z = 1$ uncoupled limit we recover the characteristic cavity frequency and decay rates $\Omega_o \equiv \sqrt{D^o_{NF}|D^o_{FN}| - D^o_{FF}D^o_{NN}}$ and $\Gamma_o \equiv (D^o_{NN} + D^o_{FF})/2$,

$$\Omega_o = \sqrt{v_g\mu\frac{g_rF_o}{N_o}} = \left\{\gamma v_g\mu\frac{N_J/N_o - \tilde{\gamma}/\gamma}{\ln(N_o/N_{tr})}\right\}^{1/2} \tag{56}$$

$$\Gamma_o = -\frac{\gamma+\tilde{\gamma}}{2}. \tag{57}$$

For usual VCSEL parameters Γ is much smaller than Ω, scaling as $\Gamma/\Omega \simeq \Gamma_o/\Omega_o \simeq \sqrt{\gamma/v_g\zeta\mu} \ll 1$, so one may set the square root in (53) to unity.

Proceeding to the full stability treatment we include out-of-phase variations in the field, allowing perturbation in the phase difference among sites $\delta\Phi \neq 0$ and consequently $D_{N\Phi}, D_{F\Phi}, D_{\Phi\Phi} \neq 0$. Since the resulting characteristic equation from the 3×3 determinant (51) is cubic, one root remains real: no additional oscillatory (i.e. complex) branch is introduced and the qualitative behavior of the system stays the same. The main impact is in the stability of the steady state, since the real root now assumes a finite value, $\lambda_3 \neq 0$. Algebraic solution of the third order characteristic equation yields the three roots

$$\lambda_{1,2} = 2\sqrt{\frac{|P|}{3}}\left(\cos\left(\frac{2\pi}{3}\right)\frac{\mathcal{C}}{3} \pm i\sin\left(\frac{2\pi}{3}\right)\right) + \frac{A_2}{3} \tag{58}$$

$$\lambda_3 = 2\sqrt{\frac{|P|}{3}}\frac{\mathcal{C}}{3} + \frac{A_2}{3} \tag{59}$$

where $A_2 \equiv D_{NN} + D_{FF} + D_{\Phi\Phi}$, $\mathcal{C} = -\mathrm{sign}(Q)\sqrt{27|Q|^2/4|P|^3}$, and P, Q are given in terms of the matrix elements D_{XY} in Appendix B. For the usual scaling $\Gamma/\omega \ll 1$ we have $A_2 < 0$ and $P > 0$ over the entire operation region. The complex plane location of the roots is then determined by the sign of Q, as depicted schematically in Figures 13a and 13b for $Q < 0$ and $Q > 0$ respectively. Hence, by inspection, the real root stability $\lambda_3 < 0$, or the complex root stability $\Re\lambda_{1,2} < 0$, are *sufficient* for global stability for, respectively, $Q < 0$ and $Q > 0$

$$\lambda_3 < 0 \quad \text{and} \quad Q < 0 \tag{60}$$

$$\Re\lambda_{1,2} < 0 \quad \text{and} \quad Q > 0. \tag{61}$$

More specifically, for low values of the coupling strengths, corresponding to small size phase perturbation elements $D_{X\Phi}$, we have $Q < 0$, corresponding to the shaded portion of the parameter space contour plot Figure 14a. Here, according to the root diagram 13a, the real root stability condition $\lambda_3 < 0$ is *sufficient* for global stability, because $\Re\lambda_{1,2} \le \lambda_3 < 0$. We know that, in the zero Φ-variation limit equation (52), $\lambda_3 = 0$, hence

$$2\sqrt{\frac{|P_o|}{3}}\frac{3}{2}\sqrt{\frac{|Q_o|^2}{|P_o|^3}} + \frac{D_{NN}+D_{FF}}{3} = 0 \tag{62}$$

P_o, Q_o being the zero Φ-variation limits of P, Q. Thus, in order to keep $\lambda_3 < 0$ the induced change $\delta\lambda_3$ due to finite $D_{X\Phi}$ terms must be negative. Expanding P, Q in (59) around P_o, Q_o in the small quantities $D_{X\Phi}$ relative to Ω^2,

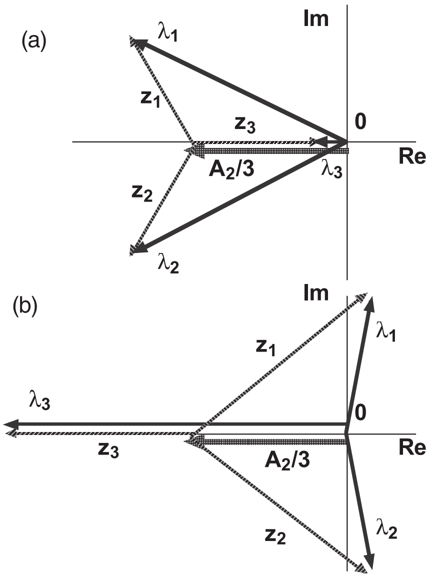

Fig. 13. Roots of the cubic characteristic equation in the complex plane (a) for $Q > 0$ the stability of the real root $\lambda_3 < 0$ is sufficient for global stability (negative real parts for the two conjugate roots $\lambda_{1,2}$), (b) for $Q > 0$ the real parts of $\lambda_{1,2}$ will turn positive, regardless of $\lambda_3 < 0$.

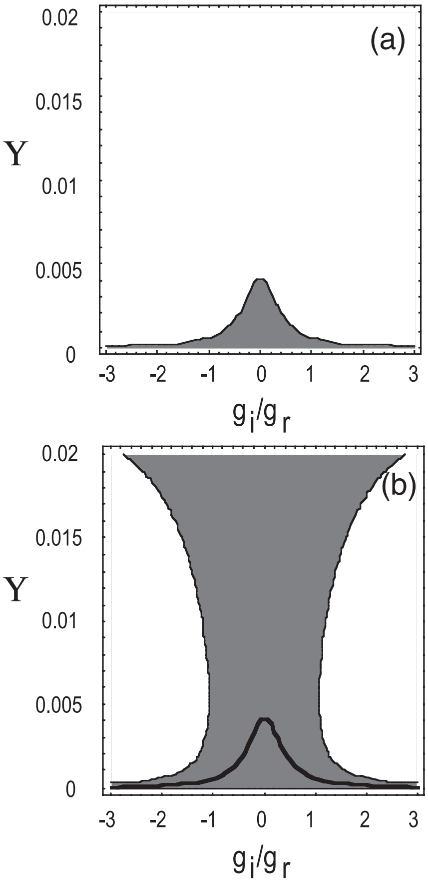

Fig. 14. Area (shaded) of negative $Q < 0$ in $g_i/g_r - \Upsilon$ parameter space. Unconditional root stability in this area. (b) Total stability area (shaded) below and above $Q = 0$. Solid line marks the transition $Q = 0$. Conditional stability extends for $Q > 0$.

and substituting for $D_{X\Phi}$ keeping leading contributions up to order $\Upsilon, V \sim \epsilon$, yields

$$\delta\lambda_3 = 4\Upsilon v_g \mu \left(\frac{g_i^2}{g_r^2}(1 - \cos \kappa b) - 1\right)(1 - \cos \kappa b) \cos Kb \tag{63}$$

where without loss of generality we let $K_{x,y} = K, \kappa_{x,y} = \kappa$, and $b_{x,y} = b$. Since at steady state $\Upsilon \cos Kb > 0$ the stability condition $\delta\lambda_3 < 0$ for the most unstable perturbation $\kappa b = \pi$ becomes,

$$\frac{g_i^2}{g_r^2} - \frac{1}{2} < 0. \tag{64}$$

Thus, for small values of the phase-perturbation effects, expressed by the condition $Q < 0$, there is unconditional stability regardless of coupling strength Υ, for $g_i < g_r/\sqrt{2}$.

At higher coupling strengths Q turns positive when (Appendix B)

$$8\Upsilon < \frac{1}{3}\left[\frac{\tilde{\gamma} + \gamma_R}{v_g \mu} - 8(\Upsilon^{\dagger} - \frac{\alpha}{\mu}V)\right] \Big/ \left(\frac{1}{3} + 2\frac{g_i^2}{g_r^2}\right) \tag{65}$$

above the shaded area boundary in Figure 14a. Crossing into the positive $Q > 0$ occurs at lower Υ with increasing ratio g_i/g_r. The Υ value for Q sign reversal is finite at $g_i = 0$. The complex root topology flips to that of Figure 13b, hence in the high coupling strength area the roots of the 3×3 matrix cannot be obtained by linear expansions around the no-phase perturbation 2×2 case, as was done for Figure 13a. Since we now have $\lambda_3 < \Re\lambda_{1,2}$ the sufficient stability condition reads

$$\Re\lambda_{1,2} = 2\sqrt{\frac{|P|}{3}}\frac{1}{2}\sinh\left[\frac{\sinh^{-1}|\mathcal{C}|}{3}\right] + \frac{A_2}{3} < 0. \tag{66}$$

This condition is not automatically satisfied with the right choice for the steady-state phase $\Upsilon \cos Kb > 0$. The stability region for $Q > 0$ is marked by the shaded area located above the solid line $Q = 0$ in Figure 14b. Unstable oscillations break out above the shaded region. As a general remark, instability always involves the complex roots crossing into $\Re\lambda_{1,2} > 0$, while the real root λ_3 remains stable over the entire parameter space. This is shown in Figures 15a and 15b, plotting the real parts from (58, 59) vs. g_i/g_r for various strengths Υ.

The entire stability region in the $g_i/g_r, \Upsilon$ space, obtained by exact calculation of the roots (58, 59) is shown by the shaded area in Figure 16a. The parameters held fixed are $\gamma = 2 \times 10^9$ s^{-1}, $v_g = 10^{10}$ cm/s, $\mu = 80$ cm^{-1}, $g_r = 1300$ cm^{-1} $\zeta = 0.065$ and $I/I_{th} = 5$. The shape of Figure 16a is typical over a wide parameter range and the stability rules can be summarized as follows. There is a complex gain range $|g_i/g_r| \leq \beta$ characterized by unconditional lattice stability, regardless of the coupling strengths Υ, $\mathcal{G}$. Outside that range, the stability is conditional, for coupling strengths below a threshold value $\Upsilon \leq \Upsilon_S(g_i/g_r)$ given by (65). The width β of the unconditional stability region, and the stable area size in general, decreases with increasing laser bias, as shown in Figure 16b for $I/I_{th} = 10$. On the other hand, stability increases with

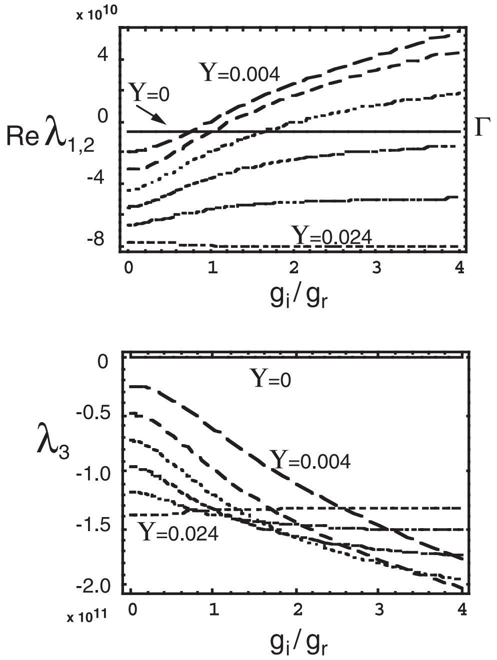

Fig. 15. Real parts of the roots of the stability matrix vs. phase perturbation strength g_i/g_r for various coupling strengths Υ, (a) complex pair $\Re\lambda_{1,2}$, (b) real root $\Re\lambda_3 = \lambda_3$. Only the complex pair enters $Re > 0$ for large phase perturbation strength.

reduced group velocity, as depicted in Figure 16c with $v_g = 10^8$ cm/s. The stability area is always symmetric in $\pm g_i$. Notably it is solely the absolute ratio of the linewidth factor to the real gain $|g_i/g_r|$ that defines the limit for *unconditional* lattice stability to perturbations, regardless of the coupling strength value.

Earlier lattice stability analysis [1] has also attributed the onset of instability to the complex roots crossing into the positive half-plane. However the earlier 2×2 dispersion limit is strictly valid for $\Upsilon \ll 1$, where $Q < 0$ and the present analysis predicts stability. Phase perturbations were also ignored in the stability analysis for two coupled cavities [10]. In general the 2×2 limit puts the stability boundary near the $Q = 0$ curve shown in Figure 13. The full 3×3 matrix roots are thus necessary to pinpoint the stability boundaries, while previous results serve as qualitative estimates. Because earlier simulations covered the large $g_i/g_r \simeq 4$ regime they did not find the unconditional stability range $g_i/g_r \leq \beta$.

Our numerical simulations have so far confirmed the validity of the present stability conclusions. Stable phase locking in the unconditional stability regime occurs for coupling strength values approaching unity, up to the weak coupling approximation limit. Any externally excited lattice wave of real wavenumber κ' is a stable perturbation of real frequency $\omega(\kappa')$ that decays in time with decay rate $\Gamma(\kappa')$. Stable locking is also achieved in the conditional region $|g_i/g_r| > \beta$ for small coupling strengths Υ. (A second stability region predicted at high coupling $\Upsilon \geq \Upsilon_{SS}$ is not borne out by simulations, most likely because the linear analysis breaks down there.) The character of the stable dispersion however changes in going from the unconditional to the conditional stability region. Figure 17a shows contour plots of the lattice dispersion for $g_i/g_r < \beta$ using the exact 3×3 matrix eigenvalues (58) around the $K_x b_x = K_y b_y = 0$ steady-state. The oscillation frequency $\Omega(\kappa_x b_x)$, plotted in Figure 17b, remains sinusoidal at relatively high strengths.

Similar conclusions follow from the real part (decay rate) $\Gamma(\kappa_x b_x)$, plotted in Figures 17c and 17d. In fact, in the unconditional stability region the roots show the same qualitative behavior as the 2×2 roots (54, 55) obtained by neglecting phase perturbations. The lattice dispersion becomes profoundly non-linear in the regime $g_i/g_r > \beta$, as shown in Figure 18. Both the oscillation frequency $\Omega(\kappa_x b_x)$, Figures 18a and 18b, and the growth rate Figures 18c and 18d, exhibit high unharmonic content, although the coupling strengths Υ are the *same* as in Figure 17. This underscores the paramount importance of the phase-perturbation effects parameterized by the ratio g_i^2/g_r^2. Large phase-pushing factors determine the strength

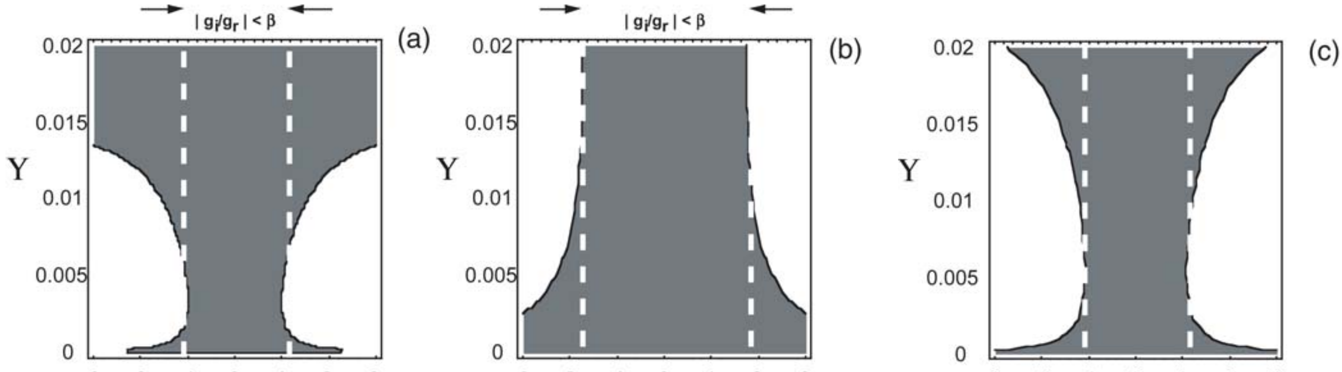

Fig. 16. Effects of various parameters on the stability regime. Same values as in Figure 15b, except (a) bias current reduced from 10 to 5 I_{th}, (b) group velocity reduced from 1×10^9 to 1×10^8 cm/s, (c) intercavity absorption added with $V = 2\Upsilon$.

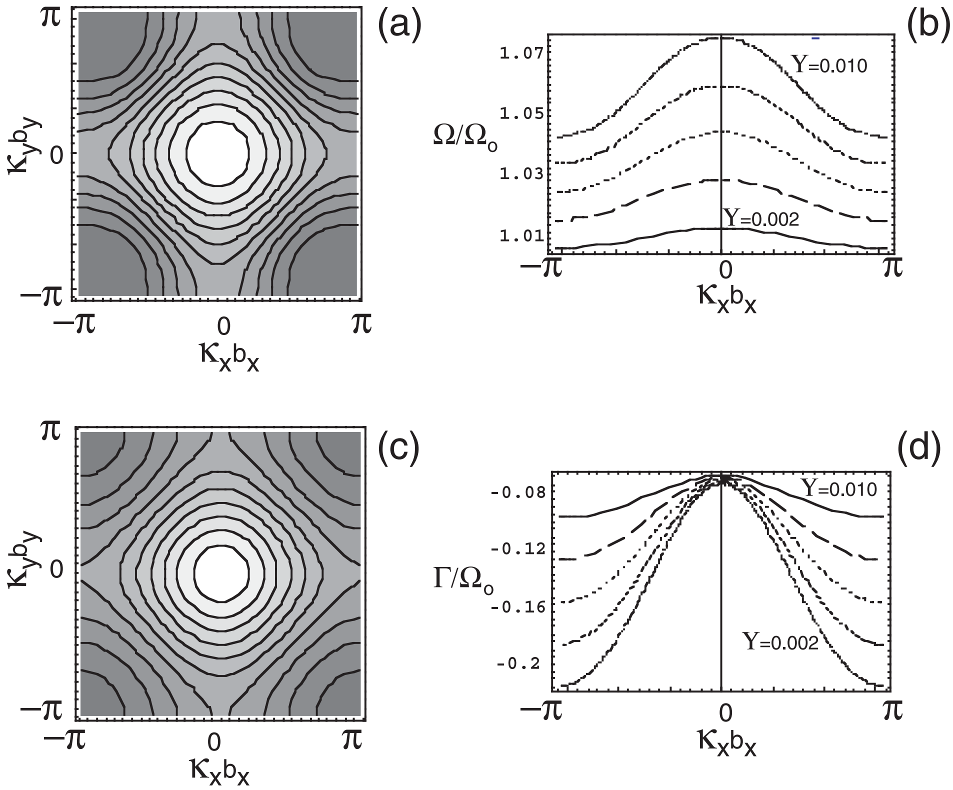

Fig. 17. Lattice wave dispersion relation for small phase perturbation factor $g_i/g_r = 6/13$, at steady-state with $Kb = K_y b = 0$. (a) Contour plots Ω/Ω_o vs. $\kappa_x b_x$, $\kappa_y b_y$ at coupling strength $\Upsilon = 0.010$. (b) Line plots $\Omega(k_x b)/\Omega_o$ along the line $k_y b_y = 0$ for equidistant coupling strengths between $\Upsilon = 0.002$ and $\Upsilon = 0.010$. (c) Contour plots γ/Ω_o vs. $\kappa_x b_x, \kappa_y b_y$, at coupling strength $\Upsilon = 0.010$. (d) Line plots $\gamma(k_x b)/\Omega_o$ along the line $k_y b_y = 0$ for equidistant coupling strengths between $\Upsilon = 0.002$ and $\Upsilon = 0.010$. the dispersion is nearly sinusoidal resembling the 2×2 roots.

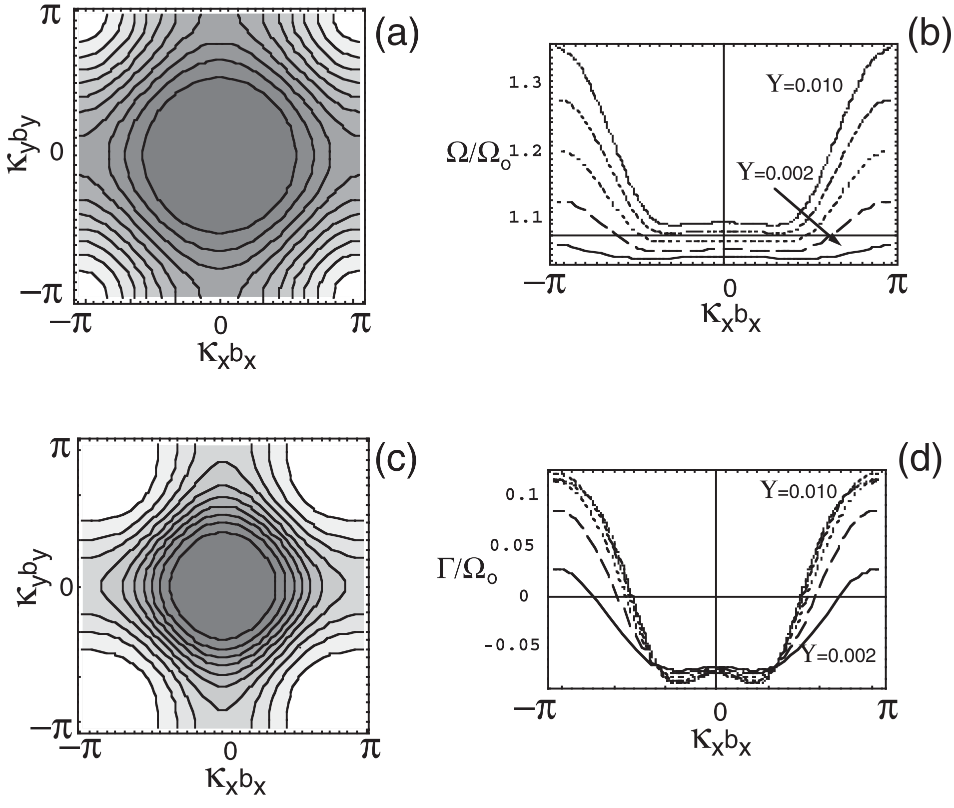

Fig. 18. Lattice wave dispersion relation for high phase perturbation factor $g_i/g_r = 2$, at steady-state with $Kb = K_y b = 0$. (a) Contour plots Ω/Ω_o vs. $\kappa_x b_x, \kappa_y b_y$ at coupling strength $\Upsilon = 0.010$. (b) Line plots $\Omega(k_x b)/\Omega_o$ along the line $k_y b_y = 0$ for equidistant coupling strengths between $\Upsilon = 0.002$ and $\Upsilon = 0.010$. (c) Contour plots γ/Ω_o vs. $\kappa_x b_x, \kappa_y b_y$, at coupling strength $\Upsilon = 0.010$. (d) Line plots $\gamma(k_x b)/\Omega_o$ along the line $k_y b_y = 0$ for equidistant coupling strengths between $\Upsilon = 0.002$ and $\Upsilon = 0.010$. The dispersion is clearly non-linear even at low Υ.

of nonlinear effects under given coupling strengths. The most unstable perturbations $\Gamma > 0$ in Figure 18d correspond to oscillation wavenumbers $\kappa b \simeq \pm\pi$, thus $\kappa b = \pi$ was employed for the stability boundaries in Figures 14 and 16.

The conditional stability regime shows intense nonlinear behavior above the stability threshold $\Upsilon > \Upsilon_S$. The values $\Delta\tilde{\varphi}_o(t)$, $F_o(t)$ exhibit transitions to stable non-linear periodic orbits (*limit cycles*), and undergo successive period-doublings leading eventually to spatiotemporal chaotic behavior [19].

Complex oscillation frequencies of real wavenumber κ, dispersion (53), apply to the time evolution of initial value problems and superpositions of real wavenumber modes. Space propagation in boundary value problems with imposed, time-dependent, boundary conditions, is also of interest. A real driving frequency leads to complex wavenumbers $\kappa \to \kappa + i\eta$ and evanescent waves, where the decay constant $\eta(\Omega)$ is found by solving equation (53) for $\Im\Theta(\kappa + i\eta) = 0$ under given $\Omega = \Re\Theta(\kappa + i\eta)$. Propagation of spatially decaying modes, excited by externally driving selected sites in the array, has been described elsewhere [20].

The so far stability discussion was based on the scaling $\Omega_o/\Gamma \sim \Omega_o/\gamma \simeq \sqrt{v_g\mu/\gamma} \gg 1$ for most manufactured VCSELs. For the opposite case $\omega_o/\gamma \simeq \sqrt{v_g\mu/\gamma} \ll 1$, involving combinations of low group velocity and very low cavity losses (large carrier decay rate γ is unwanted) both roots of equation (58) remain real and negative, with $-\Gamma < 0$, regardless of Υ. Pure damping of fluctuations and unconditional stability is now extended over the entire parameter space.

6 Passively coupled cavity limit

Fringe-field coupling among “passive” cavities (no gain medium) is finding applications for coupled-cavity waveguides in photonic crystal structures. The presented active coupling theory is reduced to the passive cavity limit by discarding the carrier density equation (35), and by dropping all gain terms $g_{r,i} = 0$ from the field equations (36, 37). The reduced amplitude and phase equations are

$$\begin{aligned}\frac{dF_{ij}}{dt} = {}& -v_g\mu F_{ij} - \sum_{i'=i\pm1}\sum_{j'=j\pm1}\left(\Lambda^\dagger v_g\mu + \Pi\frac{v_g}{2}\delta\hat{\alpha}\right)F_{ij} \\ & - \sum_{i'=i\pm1}\sum_{j'=j\pm1}\left(V2v_g\delta\hat{\alpha} + \Upsilon^\dagger 2v_g\mu\right) \\ & \times\sqrt{F_{ij}F_{i'j'}}\cos\Delta\varphi^{\pm}_{i,j} \\ & - \sum_{i'=i\pm1}\sum_{j'=j\pm1}\Upsilon 2\omega\delta\hat{\epsilon}\sqrt{F_{ij}F_{i'j'}}\sin\Delta\varphi^{\pm}_{i,j} \qquad (67)\end{aligned}$$

$$\begin{aligned}\frac{d\Delta\varphi_{ij}}{dt} = {}& \sum_{i'=i\pm1}\sum_{j'=j\pm1}\Upsilon 2\frac{\omega}{2}\delta\hat{\epsilon}\left\{\sqrt{\frac{F_{i'j'}}{F_{ij}}}\cos\Delta\varphi^{\pm}_{ij}\right. \\ & \left. - \sqrt{\frac{F_{i'j'-1}}{F_{i,j-1}}}\cos\Delta\varphi^{\pm}_{i,j-1}\right\} \\ & - \sum_{i'=i\pm1}\sum_{j'=j\pm1}\left(V2\frac{v_g}{2}\delta\hat{\alpha} + \Upsilon^\dagger v_g 2\frac{\mu}{2}\right) \\ & \times\left\{\sqrt{\frac{F_{i'j'}}{F_{ij}}}\sin\Delta\varphi^{\pm}_{ij} - \sqrt{\frac{F_{i'j'-1}}{F_{i,j-1}}}\sin\Delta\varphi^{\pm}_{i,j-1}\right\}. \qquad (68)\end{aligned}$$

Here μ parameterizes intra-cavity losses (instead of mirror losses), while, as before, $\Delta\alpha$ inter-cavity absorption and $\Delta\epsilon$ dielectric coupling. There is no steady-state, since the isolated cavity modes in (67) decay in time. Yet, lossy coupled-cavity waves can propagate along the lattice provided their decay rate in time (space) is much smaller than their frequency (wavelength). Assume for example that all cavities have been initially pumped at constant amplitude F_o and phase difference $\Delta\varphi_o$, before the gain is turned off. The dispersion for the subsequent decaying collective oscillations follows from the stability analysis of perturbations around the nominal steady-state. The characteristic equation is given by the lower right 2×2 sub-determinant of (51)

$$\det\begin{vmatrix} H_{FF}-\lambda & H_{F\Phi} \\ H_{\Phi H} & H_{\Phi\Phi}-\lambda \end{vmatrix} = 0 \qquad (69)$$

where the matrix elements H_{XY} result from the corresponding D_{XY}, equation (51), by omitting gain terms. The complex frequency, for real propagation constant κ, is

$$\begin{aligned}\Theta \equiv -\Gamma + i\Omega = {}& \frac{H_{FF}+H_{\Phi\Phi}}{2} \\ & + \frac{i}{2}\sqrt{4H_{F\Phi}H_{\Phi H} - \left(H_{FF}-H_{\Phi\Phi}\right)^2}. \qquad (70)\end{aligned}$$

The diagonal terms are pure real, yielding the decay rate $\Gamma < 0$. For lattice oscillations (real Ω) the quantity under the square root must be positive. For originally in- (out-) of phase cavities $K_xb_x = K_xb_x = 0, (\pi)$ it leads to the condition (Appendix B)

$$\frac{\omega\delta\hat{\epsilon}}{v_g\mu} > \frac{1}{4} + \Lambda + (\Pi \pm V)\delta\hat{\alpha}. \qquad (71)$$

According to (71) the dielectric coupling strength among cavities must exceed the combined cavity decay and the lossy-coupling terms. In fact the oscillation frequency is entirely generated by the dielectric coupling, since the uncoupled passive cavities do not oscillate. Hence the dispersion (70) is linear, independent of the amplitude F_o, as opposed to (54–56). For practical applications the decay rates must be much lower than the frequency ω, which implies very low loss cavities.

It is of practical interest to consider wave propagation when the original "steady-state" is the vacuum $F_o = 0$. In that limit the original complex amplitude equation (25), with zero gain terms, is *the* propagation equation for the lattice perturbation $\delta\mathcal{E}_{ij} \equiv \mathcal{E}_{ij}$. Again, imposing the Bloch condition $\mathcal{E}_{ij} = \mathcal{E}_o \exp[i\boldsymbol{\kappa} \cdot \mathbf{R}_{ij}]$ and assuming near-neighbor coupling with $\mathcal{E}_{i\pm1} = \mathcal{E}_{j\pm1} = \mathcal{E}_o \exp[\pm i\boldsymbol{\kappa} \cdot \mathbf{b}]$ yields the 2-D version of the earlier introduced coupled-cavity waveguide equation

$$\begin{aligned}\frac{d\mathcal{E}_o}{dt} = -v_g\mu\mathcal{E}_o - 4\left(\mathit{\Lambda}^\dagger v_g\frac{\mu}{2} + \mathit{\Pi}\frac{v_g}{2}\delta\hat{\alpha}\right)\mathcal{E}_o \\ - 4\left(V2v_g\frac{\delta\hat{\alpha}}{2} + \mathit{\Upsilon}^\dagger 2v_g\frac{\mu}{2} + i\mathit{\Upsilon}2\omega\frac{\delta\hat{\epsilon}}{2}\right) \\ \times \mathcal{E}_o\Big(\cos\kappa_x b_x + \cos\kappa_y b_y\Big).\end{aligned} \qquad (72)$$

It yields earlier described [12] complex oscillation frequencies $\mathit{\Theta} = \mathit{\Gamma} + i\mathit{\Omega}$, where

$$\begin{aligned}\mathit{\Gamma} = -v_g\Bigg[(1+4\mathit{\Lambda})\mu + 4\mathit{\Pi}\frac{\delta\hat{\alpha}}{2} \\ + 8\left(V\frac{\delta\hat{\alpha}}{2} + \mathit{\Upsilon}^\dagger\frac{\mu}{2}\right)(\cos\kappa_x b_x + \cos\kappa_y b_y)\Bigg]\end{aligned} \qquad (73)$$

$$\mathit{\Omega} = 8\mathit{\Upsilon}\omega\frac{\delta\hat{\epsilon}}{2}(\cos\kappa_x b_x + \cos\kappa_y b_y). \qquad (74)$$

The real frequency part $\mathit{\Omega}$ is provided solely by the real dielectric coupling. For practical applications requiring $\mathit{\Omega} \gg \mathit{\Gamma}$ the dielectric coupling must exceed the combined intra and inter cavity losses, $\mathit{\Upsilon}\mathit{\Delta}\epsilon/\mathit{\Upsilon}^\dagger\mu, \mathit{\Upsilon}\mathit{\Delta}\epsilon/V\mathit{\Delta}\alpha \gg 1$. The same condition permits propagation of decaying lattice waves (complex propagation constant $\kappa = \kappa_o + i\nu$) of real frequency, $\mathit{\Theta} = \mathit{\Omega}$.

7 Conclusion

A most general model for weakly coupled microlaser lattices, addressing both passive and active cross-cavity interactions, has been introduced and analyzed. Spontaneous relaxation to periodic Bloch states for infinite arrays, with boundary layers for finite arrays, was numerically and analytically demonstrated. The observed phase selection among adjacent lattice sites is consistent with gain maximization through interactions. The excitation and stability of lattice oscillations was analyzed. For the weak coupling, near-neighbor interaction regime under consideration, lateral interactions generate narrow frequency propagating passbands out of localized (non-propagating) cavity modes. Both absolute and conditional stability regimes for the active lattice oscillations were identified; the first depends on the imaginary part of the gain, the second on the inter-cavity coupling strength. In the conditional stability regime we observed periodic cycles and finally chaotic spatio-temporal lattice oscillations for increasing *coupling strength* $\mathit{\Upsilon}$ under constant in time uniform in space bias. Increasing the common driving laser bias between the top and bottom of the array actually stabilizes lattice oscillations (provided single mode operation is imposed on each cavity).

High values of coupling strength are desirable in practical applications to overcome random or systematic variations in the cold cavity parameters due to manufacturing tolerances. One would then seek materials with $\iota < 1$ to allow unconditional dynamic stability for large coupling $\mathit{\Upsilon}$. The ι value is a material parameter which also depends on quantum confinement effects. Use of quantum dots has already yielded $\iota < 1$ in GaAs based structures.

Appendix A: Lattice-orthogonal basis and coupling coefficients

Strictly speaking the original GL basis functions are not lattice-orthogonal

$$\int_0^\infty d^2rU^*(\mathbf{r} - \mathbf{R}_{ij})U(\mathbf{r} - \mathbf{R}_{i'j'}) \neq \delta_{i,i'}\delta_{j,j'}.$$

An orthonormal basis $U \rightarrow \hat{U}$ is readily constructed following the Gramm-Schmidt orthogonalization procedure. Limiting interactions to nearest neighbors with $\mathbf{R}_{i'-i,j'-j} = \pm\mathbf{b}_{x,y}$ we obtain expressions (8, 9). For Gaussian cavity eigenmodes and using dimensionless rectangular coordinates $\bar{x} = x/w, \bar{y} = y/w, \bar{b} = b/w$

$$\begin{aligned}C_{\pm x} &= \frac{2}{\pi}\int_\infty^\infty d\bar{y}\int_\infty^\infty d\bar{x}e^{-2\bar{y}^2}e^{-2[\bar{x}^2\pm2\bar{x}\bar{y}+\frac{\bar{b}^2}{2}]} \\ &= \frac{2}{\pi}e^{-\frac{\bar{b}^2}{2}}\int_\infty^\infty d\bar{y}e^{-2\bar{y}^2}\int_\infty^\infty d\bar{x}e^{-2[\bar{x}\mp\frac{\bar{b}}{2}]^2} = e^{-\frac{\bar{b}^2}{2}}.\end{aligned} \qquad (A.1)$$

For weak coupling the cavity separation is at least three times the mode waist $b/w \geq 3$ and $C_{x,y}$ is less than 10^{-2}. Terms of order C^2, being equivalent to second neighbor interaction strengths, are henceforth neglected and the normalization constant for $\hat{U}$ (equal to $\sqrt{1 - 3C^2/2 + C^4/2}$ for 1-D, etc.) is set to unity. First we examine the effect of the normalization on the exact cavity eigenmode equation

$$\left[\nabla_\perp^2 - k^2 + \frac{\omega^2}{c^2}\left(\epsilon_o + \delta\epsilon\chi(\mathbf{r})\right)\right]U(\mathbf{r}) = 0. \qquad (A.2)$$

Applying stationary perturbation theory to (A.2), the frequency correction introduced by the use of $\hat{U}$, equation (8), in place of U, is given by

$$\begin{aligned}\delta\left(\frac{\omega^2}{c^2}\epsilon_o\right) = 2\frac{\delta\omega}{\omega}\frac{\omega^2}{c^2}\epsilon_o = -\frac{1}{2N_D}\sum_{\pm x}\sum_{\pm y}C_{x,y}\epsilon_o \\ \times\int_0^\infty d^2\mathbf{r}U^*(\mathbf{r})\frac{\omega^2}{c^2}\chi(\mathbf{r})U(\mathbf{r} \mp \mathbf{b}_{x,y}).\end{aligned} \qquad (A.3)$$

The integral in the rhs is just the definition of $C_{x,y}$, yielding a second order correction in frequency

$2\delta\omega/\omega = -C_{x,y}^2/2$ which can be neglected. Next, the hatted basis $\hat{U}$ is used for the coupling coefficients definitions $\varUpsilon$, $\varLambda$, equations (27) and (28), and assuming for simplicity square lattice with $C_x = C_y = C$, yields

$$\begin{aligned}\varUpsilon_{\pm 1} \equiv \varUpsilon &= \int_0^{2\pi} d\theta \int_0^{\infty} dr\, r\hat{U}(\mathbf{r})\chi(\mathbf{r})\hat{U}(\mathbf{r}\mp\mathbf{b}) \\ &= 2\pi \int_0^{\infty} drr\Big\{U(\mathbf{r})\chi(\mathbf{r})U(\mathbf{r}\mp\mathbf{b}) - \frac{C}{2N_D} \\ &\times \big[U(\mathbf{r}\mp\mathbf{b})\chi(\mathbf{r})U(\mathbf{r}\mp\mathbf{b}) \\ &+ U(\mathbf{r})\chi(\mathbf{r})U(\mathbf{r}) + U(\mathbf{r})\chi(\mathbf{r})U(\mathbf{r}\mp 2\mathbf{b}) \\ &+ U(\mathbf{r}\pm\mathbf{b})\chi(\mathbf{r})U(\mathbf{r}\mp\mathbf{b})\big] + \mathcal{O}(C^2)\Big\}. \end{aligned} \tag{A.4}$$

Second order contributions from cavities two lattice sites apart (i.e. $U(\mathbf{r})U(\mathbf{r}\mp 2\mathbf{b})$ and $U(\mathbf{r}\pm\mathbf{b})U(\mathbf{r}\mp\mathbf{b})$) are dropped. The contribution $\propto C\int U^2(\mathbf{r}\mp\mathbf{b})\chi(\mathbf{r}) = C\varLambda$ is also second order. Thus, and employing similar procedure for the rest overlap factors, yields

$$\begin{aligned}&\varUpsilon = \mathcal{Y} - \frac{1}{2N_D}C\mathcal{Q} \qquad \varLambda = \varLambda - \frac{N_D}{2N_D}C\mathcal{Y} + \frac{C^2}{4N_D^2}\mathcal{Q} \\ &V = \mathcal{V} - \frac{2N_D}{2N_D}C\varPi \qquad \varPi = \varPi - \frac{2N_D}{2N_D}C\varPi \end{aligned} \tag{A.5}$$

where

$$\mathcal{Q} = \int_0^{2\pi} d\theta \int_0^{\infty} dr\, rU^2(\mathbf{r})\chi(\mathbf{r}) \tag{A.6}$$

is the cavity “transverse confinement” factor, of order unity, and

$$\mathcal{Y} = \int_0^{2\pi} d\theta \int_0^{\infty} dr\, rU(\mathbf{r})\chi(\mathbf{r})U(\mathbf{r}\mp\mathbf{b}) \tag{A.7}$$

$$\varLambda = \int_0^{2\pi} d\theta \int_0^{\infty} dr\, rU^2(\mathbf{r}\mp\mathbf{b})\chi(\mathbf{r}) \tag{A.8}$$

$$\begin{aligned}\mathcal{V} &= \int_0^{2\pi} d\theta \int_0^{\infty} dr\, rU(\mathbf{r})\chi(\mathbf{r}\mp\mathbf{b}/2)U(\mathbf{r}\mp\mathbf{b}) \\ &= \int_0^{2\pi} d\theta \int_0^{\infty} dr\, rU\left(\mathbf{r}\pm\frac{\mathbf{b}}{2}\right)\chi(\mathbf{r})U\left(\mathbf{r}\mp\frac{\mathbf{b}}{2}\right)\end{aligned} \tag{A.9}$$

$$\begin{aligned}\varPi &= \int_0^{2\pi} d\theta \int_0^{\infty} dr\, rU^2(\mathbf{r}\mp\mathbf{b})\chi\left(\mathbf{r}\mp\frac{\mathbf{b}}{2}\right) \\ &= \int_0^{2\pi} d\theta \int_0^{\infty} dr\, rU^2\left(\mathbf{r}\mp\frac{\mathbf{b}}{2}\right)\chi(\mathbf{r}).\end{aligned} \tag{A.10}$$

The far rhs in (A.9–A.10) derives from a half-period origin shift by $\mathbf{b}/2$. The mixing among mid-lattice centered terms, i.e.

$$\begin{aligned}V_{\pm 1} \equiv V = 2\pi \int_0^{\infty} dr\, r\Bigg\{&U\left(\mathbf{r}\pm\frac{\mathbf{b}}{2}\right)\chi(\mathbf{r})U\left(\mathbf{r}\mp\frac{\mathbf{b}}{2}\right) \\ &- \frac{C}{2N_D}\Bigg[U\left(\mathbf{r}\pm\frac{\mathbf{b}}{2}\right)\chi(\mathbf{r})U\left(\mathbf{r}\pm\frac{\mathbf{b}}{2}\right) \\ &+ U\left(\mathbf{r}\pm 3\frac{\mathbf{b}}{2}\right)\chi(\mathbf{r})U\left(\mathbf{r}\mp\frac{\mathbf{b}}{2}\right) \\ &+ U\left(\mathbf{r}\pm\frac{\mathbf{b}}{2}\right)\chi(\mathbf{r})U\left(\mathbf{r}\mp 3\frac{\mathbf{b}}{2}\right) \\ &+ U\left(\mathbf{r}\pm\frac{\mathbf{b}}{2}\right)\chi(\mathbf{r})U\left(\mathbf{r}\pm\frac{\mathbf{b}}{2}\right)\Bigg] + \mathcal{O}(C^2)\Bigg\}\end{aligned}$$

produces only second order corrections $\propto C\int U^2(\mathbf{r}\mp\mathbf{b}/2)\chi(\mathbf{r}) = C\varPi$ (and similar for $\varPi$).

Using the fundamental mode profiles $U_{00}(\mathbf{r}) = \sqrt{2/\pi w^2}\exp(-r^2/w^2)$, using $(\mathbf{r}-\mathbf{b}_x)^2 = (x-b_x)^2 + y^2$, $(\mathbf{r}-\mathbf{b}_y)^2 = (y-b_y)^2 + x^2$ and converting to $x = \rho\cos\phi$, $y = \rho\sin\phi$, yields

$$Q = \frac{4}{w^2}\int_0^a d\rho\rho e^{-2\rho^2/w^2} = 1 - \exp[-2a^2/w^2] \tag{A.11}$$

$$\mathcal{Y}_{x,y} = 4e^{-b_{x,y}^2/w^2}\frac{1}{w^2}\int_0^a d\rho\rho e^{-2\rho^2/w^2}\mathcal{I}_o\left(2b_{x,y}\rho/w^2\right), \tag{A.12}$$

$$\varLambda_{x,y} = 4e^{-2b_{x,y}^2/w^2}\frac{1}{w^2}\int_0^a d\rho\rho e^{-2\rho^2/w^2}\mathcal{I}_o\left(4b_{x,y}\rho/w^2\right), \tag{A.13}$$

$$\mathcal{V}_{x,y} = 4e^{-b_{x,y}^2/2w^2}\frac{1}{w^2}\int_0^a d\rho\rho e^{-2\rho^2/w^2} = Qe^{-b_{x,y}^2/2w^2} \tag{A.14}$$

$$\varPi_{x,y} = 4e^{-b_{x,y}^2/2w^2}\frac{1}{w^2}\int_0^a d\rho\rho e^{-2\rho^2/w^2}\mathcal{I}_o\left(2b_{x,y}\rho/w^2\right). \tag{A.15}$$

We have generalized for rectangular lattices with $b_x \neq b_y$. The un-normalized coupling strengths (A.12, A.15) are positive. Among the orthonormalized coupling strengths $\varLambda_{x,y}$, $V_{x,y}$ and $\varPi_{x,y}$ are always positive.

Appendix B: Stability equations around fixed points

Equations (35, 36) are expanded around the steady-state values $F_{ij} = F_o$, $N_{ij} = N_o$, $\varDelta\varphi_{ij} = \varDelta\varphi_o$. Due to periodicity an arbitrary (i,j) is chosen as reference; we take $i = j = 0$ with near neighbors $i' = \pm 1$, $j' = \pm 1$. The perturbations are themselves Bloch waves, meaning that the next site perturbations are phase shifted by κb relative to the reference site, $\delta A_{0,\pm 1} = \delta A_{\pm 1,0} = \delta A_o \exp[\pm i\kappa b]$ where A stands for F or N. Reviving $\cos\varDelta\varphi_o = (\exp[iKb] + cc)/2$ and taking the variation in respect to $\delta F, \delta N$, using the notation $D_{XY} \equiv \partial(\dot{X})/\partial Y$ with X, Y being either of δN, $\delta \mathcal{E}$ yields

$$\begin{aligned} D_{NN} &= -\gamma - 2BN_o - \frac{g_r F_o}{N_o}\left[(1+2\varLambda_x)\right. \\ &\quad \left. + (2\varUpsilon_x \cos K_x b)(1+1) + (x \to y)\right] \qquad \text{(B.1)} \\ D_{NF} &= -g_r \ln\left(\frac{N_o}{N_{tr}}\right)\Big[1+2\varLambda_x \cos\kappa_x b + 2\frac{1}{2}(2\varUpsilon_x \cos K_x b) \\ &\quad \times (1+\cos\kappa_x b) + (x \to y)\Big] \qquad \text{(B.2)} \\ D_{FN} &= v_g \zeta \frac{F_o}{N_o}\Big[g_r(1+2\varLambda_x \cos\kappa_x b) \\ &\quad + \hat{g}(2\varUpsilon_x \cos K_x b \cos\vartheta)(1+\cos\kappa_x b) + (x \to y)\Big] \qquad \text{(B.3)} \\ D_{FF} &= -v_g\mu + v_g\zeta \ln\left(\frac{N_o}{N_{tr}}\right)\Big[g_r(1+2\varLambda_x) \\ &\quad + \hat{g}2\frac{1}{2}(2\varUpsilon_x \cos K_x b \cos\vartheta)(1+\cos\kappa_x b) + (x \to y)\Big] \\ &\quad - v_g \delta\hat{\alpha}\Big[2\varPi_x + 2\frac{1}{2}(2V_x \cos K_x b) \\ &\quad \times (1+\cos\kappa_x b) + (x \to y)\Big] \\ &\quad + v_g\mu\Big[2\varLambda_x^{\dagger} + 2\frac{1}{2}(2\varUpsilon_x^{\dagger} \cos K_x b) \\ &\quad \times (1+\cos\kappa_x b) + (x \to y)\Big] \qquad \text{(B.4)} \\ D_{\varPhi N} &= v_g\zeta \frac{g_i}{2}\frac{1}{N_o}\left[(1-\cos\kappa_x b_x)\right. \\ &\quad \times (1+2\varLambda_x \cos\kappa_x b_x) + (x \to y)\Big] \\ &\quad + v_g\zeta\frac{\hat{g}}{2}\frac{1}{N_o}\left[2\varUpsilon_x(1+\cos\kappa_x b_x)\right. \\ &\quad \times \sin\vartheta\,(\cos K_x b - \cos(K_x - \kappa_x)b_x) + (x \to y)\Big] \qquad \text{(B.5)} \\ D_{\varPhi F} &= v_g\zeta\frac{\hat{g}}{2}\frac{\ln\hat{N}_o}{F_o}\left[2\varUpsilon_x(\cos\kappa_x b_x - 1)\sin\vartheta\right. \\ &\quad \times (\cos K_x b - \cos(K_x - \kappa_x)b_x) + (x \to y)\Big] \\ &\quad + \frac{\omega}{2}\frac{\delta\hat{\epsilon}}{F_o}\varUpsilon\left[2(\cos\kappa_x b_x - 1)\right. \\ &\quad \times (\cos K_x b - \cos(K_x - \kappa_x)b_x) + (x \to y)\Big]. \qquad \text{(B.6)} \end{aligned}$$

The identity $2\cos K_x b + \cos(K_x + \kappa_x)b + \cos(K_x - \kappa_x)b = 2\cos K_x b\,(1+\cos\kappa_x b)$ was used[1], where the phase shift $\pm\kappa b$ comes from $\delta A_{\pm 1}$. The neighbor site summations also yielded $\sum_{\pm}\cos(\pm K_x b_x + \vartheta) = 2\cos K_x b_x \cos\vartheta$, etc. The $2(1/2)$ factor stems from $\partial_F\sqrt{F_o F_{\pm 1}} = (1/2)[\sqrt{F_o/F_{\pm 1}}\delta F_{\pm 1} + \sqrt{F_{\pm 1}/F_0}\delta F_0]$, where $F_{\pm 1}/F_0 = N_{\pm 1}/N_0 = 1$ from the uniformity of the steady state. For the derivatives in respect to the out-of-phase variations $\delta\varphi \equiv \delta F_{\perp}/2F_o = \delta\varPhi_o \sin k_x b$ with $\delta\varPhi_o \equiv \delta F/2F_o$, we observe that analytic continuity $\varDelta\varphi_{i,i-1} = b_x d(\delta\varphi_i)/dx$ (and similar along y) requires $\delta(\varDelta\varphi)_x = \delta\varPhi_o \cos\kappa_x b_x$ etc. Thus, expanding the perturbed values $\widetilde{\varDelta}\varphi^{\pm}_{x,y} = \varDelta\varphi_o + \delta\varPhi_o \cos(\pm\kappa_{x,y} b_{x,y})$ yields the partial derivatives

$$\begin{aligned} D_{N\varPhi} &= \hat{g}2\ln\hat{N}_o F_o \varUpsilon\left[-(1+\cos\kappa_x b_x)\right. \\ &\quad \times \sin K_x b_x \cos\vartheta + (x \to y)\Big] \qquad \text{(B.7)} \\ D_{F\varPhi} &= v_g\zeta\hat{g}2\ln\hat{N}_o F_o\varUpsilon\left[-(1+\cos\kappa_x b_x)\sin K_x b_x \cos\vartheta\right. \\ &\quad + (1-\cos\kappa_x b_x)\cos K_x b_x \sin\vartheta + (x \to y)\Big] \qquad \text{(B.8)} \\ &\quad + 2v_g\left(\mu\varUpsilon^{\dagger} - \delta\hat{\alpha}V\right)F_o\left[-(1+\cos\kappa_x b_x)\right. \\ &\quad \times \sin K_x b_x + (x \to y)\Big] \\ &\quad + 2\omega\delta\hat{\epsilon}F_o\varUpsilon\left[(1-\cos\kappa_x b_x)\cos K_x b_x + (x \to y)\right] \qquad \text{(B.9)} \\ D_{\varPhi\varPhi} &= v_g\zeta\frac{\hat{g}}{2}2\ln\hat{N}_o\varUpsilon \\ &\quad \times \left[-2(1-\cos\kappa_x b_x)\cos K_x b_x \cos\vartheta + (x \to y)\right] \\ &\quad + 2\frac{v_g}{2}\left(\mu\varUpsilon^{\dagger} - \delta\hat{\alpha}V\right) \\ &\quad \times \left[-2(1-\cos\kappa_x b_x)\cos K_x b_x + (x \to y)\right]. \qquad \text{(B.10)} \end{aligned}$$

The steady-state condition (43) further simplifies (B.4)

$$\begin{aligned} D_{FF} &= -2v_g\left(\mu\varUpsilon - \delta\hat{\alpha}V + \mu\varUpsilon^{\dagger}\right) \\ &\quad \times \left[\cos K_x b_x(1-\cos\kappa_x b_x) + (x \to y)\right] \qquad \text{(B.11)} \end{aligned}$$

where we have neglected quadratic terms $\varUpsilon^2$ by taking $\zeta g_r \ln(N_o/N_{tr}) \simeq \mu$. We have generalized for arbitrary $K_x b_x \neq K_y b_y$ and $\kappa_x b_x \neq \kappa_y b_y$. Notice that the stability matrix is independent of the real dielectric variation $\varDelta\epsilon$.

The zero gain limit $g_{r,i} = 0$ yields the matrix elements for passively coupled cavities

$$\begin{aligned} H_{FF} &= -v_g\mu - \left[2\varPi_x v_g\delta\hat{\alpha} + 2\varLambda_x^{\dagger} v_g\mu\right] \\ &\quad - \left[2V_x v_g\delta\hat{\alpha} + 2\varUpsilon_x^{\dagger} v_g\mu\right] \\ &\quad \times \left[\cos K_x b\,(1+\cos\kappa_x b) + (x \to y)\right] \qquad \text{(B.12)} \\ H_{\varPhi F} &= \frac{v_g}{2F_o}\left(\mu\varUpsilon^{\dagger} + \delta\hat{\alpha}V\right)\left[2(1-\cos\kappa_x b_x)(\sin(K_x b)\right. \\ &\quad - \sin[(K_x - \kappa_x)b_x]) + (x \to y)\Big] \\ &\quad - \frac{\omega}{2}\frac{\delta\hat{\epsilon}}{F_o}\varUpsilon\left[2(1-\cos\kappa_x b_x)(\cos(K_x b)\right. \\ &\quad - \cos[(K_x - \kappa_x)b_x]) + (x \to y)\Big] \qquad \text{(B.13)} \\ H_{F\varPhi} &= v_g(\mu\varUpsilon^{\dagger} + \delta\hat{\alpha}V) \\ &\quad \times F_o\left[(1+\cos\kappa_x b_x)\sin K_x b_x + (x \to y)\right] \\ &\quad - \omega\delta\hat{\epsilon}F_o\varUpsilon\left[2(1-\cos\kappa_x b_x)\cos(K_x b) + (x \to y)\right] \qquad \text{(B.14)} \\ H_{\varPhi\varPhi} &= 2\frac{v_g}{2}\frac{1}{2}\left(\mu\varUpsilon^{\dagger} + \delta\hat{\alpha}V\right) \\ &\quad \times \left[2(1-\cos\kappa_x b_x)\cos K_x b_x + (x \to y)\right]. \qquad \text{(B.15)} \end{aligned}$$

The matrix eigenvalues in (70) depend on the discriminant $\varDelta = 4H_{F\varPhi}H_{\varPhi F} - (H_{\varPhi\varPhi} - H_{FF})^2$. For perturbations around 0- or π-phased steady states $K_{x,y}b_{x,y} = 0, \pi$ the

---

[1] In reference [1] the result $4Y\cos\varDelta\varphi_o + 4Y\cos[\varDelta\varphi_o + \kappa b]$ ought to be corrected to $4Y\cos\varDelta\varphi_o + 2Y\cos[\varDelta\varphi_o + \kappa b] + 2Y\cos[\varDelta\varphi_o - \kappa b]$.

expressions under the square root simplify to

$$H_{F\Phi}H_{\Phi F} = \frac{1}{2}\left(2\omega\delta\hat{\epsilon}\Upsilon\right)^2\left(1-\cos\kappa b\right)^2 \times\left[1-\cos\kappa b-\frac{(\mu\Upsilon^{\dagger}+\delta\hat{\alpha}V)v_g}{\omega\delta\hat{\epsilon}\Upsilon}2\mathrm{sin}\kappa b\right] \tag{B.16}$$

$$H_{\Phi\Phi}-H_{FF} = -v_g\left\{\mu(1+4\Lambda)+4\Pi\delta\hat{\alpha} +\left[4\Upsilon^{\dagger}\mu(1+\cos\kappa b)\pm 4V\delta\hat{\alpha}\right]\left(\frac{3}{2}+\frac{1}{2}\cos\kappa b\right)\right\}. \tag{B.17}$$

Substituting in $\Delta > 0$ and taking $\kappa b \to \pi$ for the most unstable perturbation yields (71)

In the uncoupled cavity limit, letting all coupling coefficients Υ, V, Λ, $\Pi = 0$, all matrix elements vanish except the upper 2×2 submatrix. Then the stability equation follows from

$$\det\begin{vmatrix} D^o_{NN}-\lambda & D^o_{NF} \\ D^o_{FN} & D^o_{FF}-\lambda \end{vmatrix} = 0. \tag{B.18}$$

It yields the characteristic cavity relaxation oscillation frequency and damping rate given by $\Omega_o^2 = -(D^o_{FN}D^o_{NF} - D^o_{NN}D^o_{FF})$, $\Gamma_o = (D^o_{NN}+D^o_{FF})/2$, equations (56, 57). The next limit is to allow oscillations in the carrier density and radiation amplitude, without changing the relative phase among sites (Fig. 12a), i.e. $\partial(\dot{N})/\partial\Delta\varphi = \partial(\dot{F})/\partial\Delta\varphi = \partial(\dot{\Delta\varphi})/\partial\Delta\varphi = 0$. Now the 3×3 stability matrix factors into the upper 2×2 determinant times λ,

$$\det\begin{vmatrix} D_{NN}-\lambda & D_{NF} & 0 \\ D_{FN} & D_{FF}-\lambda & 0 \\ D_{\Phi N} & D_{\Phi F} & 0-\lambda \end{vmatrix} = (-\lambda)\det\begin{vmatrix} D_{NN}-\lambda & D_{NF} \\ D_{FN} & D_{FF}-\lambda \end{vmatrix} = 0 \tag{B.19}$$

(even though $D_{\Phi N} = \partial(\dot{\Delta\varphi})/\partial N$, $D_{\Phi F} = \partial(\dot{\Delta\varphi})/\partial F \neq 0$). The dispersion relation, given in (54, 55), involves modified oscillation frequency and decay rates that depend on the coupling strengths and the perturbation wavenumber κ. The third root is trivial $\lambda_3 = 0$.

We now consider characteristic determinant for the full 3×3 stability matrix

$$\det\begin{vmatrix} D_{NN}-\lambda & D_{NF} & \epsilon D_{N\Phi} \\ D_{FN} & D_{FF}-\lambda & \epsilon D_{F\Phi} \\ D_{\Phi N} & \epsilon D_{\Phi F} & \epsilon D_{\Phi\Phi}-\lambda \end{vmatrix} = 0. \tag{B.20}$$

The tag ϵ indicates small terms of leading order $\sim \Upsilon$, $V \ll 1$. The transformation

$$\lambda = z + \frac{A_2}{3} \tag{B.21}$$

where $A_2 = D_{NN}+D_{FF}+D_{\Phi\Phi}$ puts the characteristic equation $\lambda^3 - A_2\lambda^2 + A_1\lambda - A_0 = 0$ into to the form

$$z^3 + Pz + Q = 0 \tag{B.22}$$

where, keeping only terms up to order ϵ, we have

$$P = \Omega^2 - \frac{4}{3}\Gamma^2 - D_{\Phi N}D_{N\Phi} + D_{NN}D_{\Phi\Phi} - \frac{4}{3}\Gamma D_{\Phi\Phi} \tag{B.23}$$

$$Q = \Omega^2\left(\frac{2}{3}\Gamma + \frac{1}{3}D_{\Phi\Phi}\right) + \frac{2}{3}\Gamma\left(D_{NN}D_{\Phi\Phi} - D_{\Phi N}D_{N\Phi}\right) - D_{NF}D_{F\Phi}D_{\Phi N} + D_{FN}D_{NF}D_{\Phi\Phi} - \frac{8}{9}\Gamma^2 D_{\Phi\Phi} - \frac{16}{27}\Gamma^3. \tag{B.24}$$

The definitions $\Omega \equiv \sqrt{D_{NF}|D_{FN}| - D_{FF}D_{NN}}$ and $\Gamma \equiv (D_{NN}+D_{FF})/2$ from the 2×2 stability limit have been used. Coefficient P is positive, $P = |P| > 0$, over the usual VCSEL operation range $\Omega^2 \gg \Gamma^2$. The sign of Q is important and determines the root location in complex plane, Figure 13. Regrouping terms yields

$$P = \Omega^2 - \frac{4}{3}\Gamma^2 + \frac{2}{3}\mathcal{D}\Gamma \tag{B.25}$$

$$Q = \mathcal{B}^3 + \frac{2}{3}\Omega^2\Gamma + \frac{4}{9}\mathcal{D}\Gamma^2 - \frac{16}{27}\Gamma^3 \tag{B.26}$$

where

$$\mathcal{B}^3 \equiv \frac{1}{3}\Omega^2 D_{\Phi\Phi} + D_{FN}D_{NF}D_{\Phi\Phi} - D_{NF}D_{F\Phi}D_{\Phi N} \tag{B.27}$$

$$\mathcal{D} \equiv \frac{3}{2}D_{\Phi\Phi}\left(\frac{D_{NN}}{\Gamma} - \frac{4}{3}\right) = D_{\Phi\Phi}\frac{D_{NN}-2D_{FF}}{D_{NN}+D_{FF}} \tag{B.28}$$

and we focus on the stability around $K_x b_x = K_y b_y = 0, \pi$ where $D_{N\Phi} \propto sinK_{x,y}b_{x,y} = 0$. Substitution of the stability matrix elements inside (B.27) yields, keeping only leading terms in coupling strength Υ

$$\mathcal{B}^3 \simeq 4\Upsilon v_g\mu\Omega^2\left(\frac{2}{3} + \frac{g_i^2}{g_r^2}(1-\cos\kappa b)\right)\cos Kb(1-\cos\kappa b) \tag{B.29}$$

and for $Q \simeq \mathcal{B}^3 + \Omega^2\left(2\Gamma + D_{\Phi\Phi}\right)/3$

$$Q \simeq -\Omega^2\left[\frac{1}{3}(\tilde{\gamma} + \gamma_R + 4G_o v_g\mu\cos Kb(1-\cos\kappa b) - 8\Upsilon\frac{g_r F_o}{N_o}\cos Kb) - 4\Upsilon v_g\mu \times\left(\frac{2}{3} + \frac{g_i^2}{g_r^2}(1-\cos\kappa b)\right)\cos Kb(1-\cos\kappa b)\right] \tag{B.30}$$

where for simplicity we let $K_{x,y}b_{x,y} = Kb$ and $\kappa_{x,y}b_{x,y} = \kappa b$. Neglecting the term $g_r F_o^2/N_o = \omega^2/\mu v_g \ll 1$ yields the parameter space region for negative Q, equation (65).

Returning to the eigenvalues, the three roots of (B.22) are given by

$$z_j = 2\sqrt{-\frac{P}{3}}\cos(\theta + j\frac{2\pi}{3}), \quad j = 1,2,3 \tag{B.31}$$

where $\theta = (1/3)\cos^{-1}\mathcal{C}$ with $\mathcal{C} \equiv \sqrt{27/4}Q/\sqrt{-P^3}$. In our parameter regime $P > 0$, $\mathcal{C} = i\mathrm{sign}Q|\mathcal{C}|$,

$|\mathcal{C}| = \sqrt{27|Q|^2/4|P|^3}$. Then, $\theta = \pi/2 + i(1/3)\mathrm{sign}(Q)\sinh^{-1}|\mathcal{C}|$, which, after substitution inside (B.31) and (B.21) yields

$$\lambda_{1,2} = 2\sqrt{\frac{|P|}{3}}\left(-\mathrm{sign}Q\cos\left(\frac{2\pi}{3}\right)\sinh\left[\frac{\sinh^{-1}|\mathcal{C}|}{3}\right]\right.$$
$$\left.\pm\, i\sin\left(\frac{2\pi}{3}\right)\cosh\left[\frac{\sinh^{-1}|\mathcal{C}|}{3}\right]\right) + \frac{A_2}{3} \qquad \text{(B.32)}$$

$$\lambda_3 = -\mathrm{sign}Q 2\sqrt{\frac{|P|}{3}}\sinh\left[\frac{\sinh^{-1}|\mathcal{C}|}{3}\right] + \frac{A_2}{3} \qquad \text{(B.33)}$$

where

$$|\mathcal{C}|^2 = \frac{\left(\Omega^2\Gamma/2\right)^2}{\left(\Omega^2/3\right)^3}\frac{\left[\mathcal{B}^3/\Omega^2\Gamma + \frac{2}{3} + \frac{4}{9}\mathcal{D}\Gamma/\Omega^2 - \frac{16}{27}\Gamma^2/\Omega^2\right]^2}{\left[1 - \frac{4}{3}\Gamma^2/\Omega^2 + \frac{2}{3}\mathcal{D}\Gamma/\Omega^2\right]^3}. \qquad \text{(B.34)}$$

Substituting the matrix elements inside $A_2 \equiv D_{NN} + D_{FF} + D_{\Phi\Phi} = 2\Gamma + D_{\Phi\Phi}$ yields

$$A_2 = -\left[\tilde{\gamma} + \gamma_s Z(\kappa; K) + 4v_g\left(\mu G_o + \mu \Upsilon\right)\right.$$
$$\left.\times\cos Kb(1 - \cos\kappa b)\right] < 0 \qquad \text{(B.35)}$$

since at steady-state $G_o \cos Kb > 0$. Hence, for $\mathrm{sign}\, Q = -1$ or $\mathrm{sign}\, Q = 1$ determined from (65), we respectively obtain the complex plane root arrangement in Figures 13a and 13b.

To compare the full stability roots with the roots of the phase-invariant 2 × 2 limit corresponding to $D_{X\Phi} = \mathcal{B} = \mathcal{D} = 0$ we expand the roots inside the determinant (B.20) as $\lambda_i = \lambda_i^o + \epsilon\delta\lambda_i$. For the third (real) root, the 2 × 2 limit is zero,

$$\lambda_3^o = 2\sqrt{\frac{|P_o|}{3}}\sinh\left[\frac{1}{3}|\mathcal{C}_o|\right] + \frac{D_{NN} + D_{FF}}{3} = 0, \qquad \text{(B.36)}$$

and the lowest order non-zero λ_3 value for the full 3×3 case equals the first order change $\delta\lambda_3$ due to the $D_{X\Phi} \neq 0$ elements. Collecting terms $\sim \epsilon$ around $\lambda_3^o = 0$ inside (B.20) yields

$$\delta\lambda_3 = D_{\Phi\Phi} + D_{\Phi N}\frac{D_{NF}D_{F\Phi} - D_{FF}D_{N\Phi}}{\Omega_o^2 + \Gamma_o^2}. \qquad \text{(B.37)}$$

Substituting the expressions for the matrix elements and neglecting terms Γ_o^2/Ω_o^2 gives (63).

In the small phase perturbation regime the roots are further simplified by the substitution, from (B.36) $2\sqrt{P_o/3}\sinh\left[|\mathcal{C}_o|/3\right] = (D_{NN} + D_{FF})/3 \equiv \Gamma_o/3$ inside (B.32, B.33) whence

$$\lambda_{1,2} = \Gamma_o + \left(\frac{1}{2}\frac{\sqrt{P_o}B^3}{\Omega_o^3} + \frac{1}{3}D_{\Phi\Phi}\right) \mp i\sqrt{P_o}\sqrt{1 + \frac{3}{2}\frac{B^3}{\Omega_o^3}} \qquad \text{(B.38)}$$

$$\lambda_3 = \sqrt{P_o}\frac{B^3}{\Omega_o^3} + \frac{D_{\Phi\Phi}}{3}. \qquad \text{(B.39)}$$

The zero phase-variation limit $B = 0$, $D_{\Phi\Phi} = 0$ of the above recovers the expressions for the 2 × 2 stability limit.

When the phase-perturbation effects become significant as $\mathcal{B}^3$ increases, the 3 × 3 roots cannot be expressed as perturbations around the 2 × 2 roots; in particular λ_3 cannot be expressed as $\delta\lambda_3$ of the trivial root. The transition $Q \geq 0$ causes essential changes in the complex root location from Figures 13a to 13b. Now it is the complex roots that tend to become unstable and cross the real axis. This will happen if

$$\Re\lambda_{1,2} = 2\sqrt{\frac{|P|}{3}}\frac{1}{2}\sinh\left[\frac{\sinh^{-1}|\mathcal{C}|}{3}\right] + \frac{A_2}{3} > 0. \qquad \text{(B.40)}$$

The stability boundary from (66) cannot be put in a simple expression and is plotted graphically using formulas (B.32) in Figures 14 and 15.

References

1. S. Riyopoulos, Phys. Rev. A **66**, 53820 (2002)
2. J.D. Joannopoulos, R.D. Meade, J.N. Winn, in *Photonic Crystals* (Princeton University, Princeton N.J., 1995)
3. O. Painter, J. Vuckovic, A. Scherer, J. Opt. Soc. Am. B **16**, 275 (1999)
4. S. Riyopoulos, J. Opt. Soc. Am. B **19**, 1544 (2002)
5. D. Zhou, L.J. Mawst, Z. Dai, IEEE JQE **38**, 652 (2002)
6. D. Botez, A.P. Napartovich, IEEE JQE **30**, 975 (1994); D. Botez, A.P. Napartovich, IEEE JQE **32**, 2175 (1996)
7. J.K. Butler, D.E. Ackley, M. Ettenberg, IEEE JQE **21**, 458 (1990)
8. H.-J. Yoo, J.R. Hayes, E.G. Paek, A. Scherer, Y.-S. Kwon, IEEE JQE **26**, 1039 (1990)
9. S.S. Wang, H.G. Winful, Appl. Phys. Lett. **52**, 1774 (1988)
10. S.S. Wang, H.G. Winful, Appl. Phys. Lett. **53**, 1894 (1988)
11. A. Yariv, Y. Xu, R.K. Lee, A. Scherer, Opt. Lett. **24**, 711 (1999)
12. U. Peschel, A.L. Reynolds, B. Arredondo, F. Lederer, P.J. Roberts, T.F. Krauss, P.J.I. de Maagt, IEEE JSTQE **38**, 830, (2003)
13. J.P. van der Ziel, D.G. Deppe, N. Chand, G.J. Zydzik, S.N.G. Chu, IEEE JQE **26**, 1873 (1990)
14. M. Orenstein, E. Kapon, N.G. Stoffel, J.P. Harbison, L.T. Florez, J.L. Wullert, Appl. Phys. Lett. **58**, 804 (1991)
15. P.L. Gourley, M.E. Warren, G.R. Hadley, G.A. Vawter, T.M. Brennan, B.E. Hammons, Appl. Phys. Lett. **58**, 890 (1991)
16. M. Orenstein, E. Kapon, J.P. Harbison, L.T. Florez, N.G. Stoffel, Appl. Phys. Lett. **60**, 1535 (1992)
17. A. Morgan, K. Kojima, T. Mullally, G.D. Guth, M.W. Focht, R.E. Leibenguth, M. Asom, Appl. Phys. Lett. **61**, 1160 (1992)
18. S. Riyopoulos, D. Dialetis, J. Liu, IEEE JSTQE **7**, 312 (2001)
19. S. Riyopoulos, AIP Chaos **14**, 1105 (2004)
20. S. Riyopoulos, Opt. Expr. **12**, 3190 (2004)
21. S. Riyopoulos, to appear in IEEE STQE (2005)